Enhancing the Electrochemical Performance in Symmetrical Solid Oxide Cells through Nanoengineered Redox-Stable Electrodes with Exsolved Nanoparticles

Javier Zamudio-García[1,2,], Jose M. Porras-Vázquez[2], Enrique R. Losilla[2], David Marrero-López[3,*]*

[1] Department of Energy Conversion and Storage, Technical University of Denmark, Fysikvej, Building 310, 2800 Kgs., Lyngby, Denmark.

[2] Universidad de Málaga, Dpto. de Química Inorgánica, Cristalografía y Mineralogía, 29071-Málaga, Spain.

[3] Universidad de Málaga, Dpto. de Física Aplicada I, 29071-Málaga, Spain.

Keywords: Solid Oxide Cells; symmetrical electrode; spray-pyrolysis; microstructural tailoring; exsolution; nanoparticles

ABSTRACT

Symmetrical solid oxide cells (SSOCs) have recently gained significant attention for their potential in energy conversion due to their simplified cell configuration, cost-effectiveness and excellent reversibility. However, previous research efforts have mainly focused on improving the electrode performance of perovskite-type electrodes through different doping strategies, neglecting the microstructural optimization. This work presents novel approaches for the nanostructural tailoring of $(La_{0.8}Sr_{0.2})_{0.95}Fe_{1-x}Ti_xO_{3-\delta}$ ($LSFT_x$, x=0.2 and 0.4) electrodes using a single-step spray-pyrolysis deposition process. By incorporating these electrodes into a $Ce_{0.9}Gd_{0.1}O_{1.95}$ (CGO) porous backbone or employing a nanocomposite architecture with nanoscale particle size, we achieved significant improvements in the polarization resistance (R_p) compared to traditional screen-printed electrodes. To further boost the fuel oxidation performance, a Ni-doping strategy, couple with meticulous microstructural optimization, was implemented. The exsolution of Ni nanoparticles under reducing conditions resulted in remarkable R_p values as low as 0.34 and 0.11 Ω cm^2 in air and wet H_2 at 700 ºC, respectively. Moreover, an electrolyte-supported cell with symmetrical electrodes demonstrated a stable maximum power density of 617 mW cm^{-2} at 800 ºC. These findings highlight the importance of combining electrode composition optimization with advanced morphology control in the design of highly efficient and durable SSOCs.

1. Introduction

Solid oxide cells (SOCs) have emerged as promising eco-friendly energy conversion devices, enabling the reversible production of electricity through electrochemical reactions using a variety of fuels.[1] To enhance the commercial viability of SOCs, researchers are actively exploring novel and efficient materials, as well as optimizing electrode architectures to lower operating temperatures and overall costs.[2,3]

In recent times, symmetrical solid oxide cells (SSOCs) have gained significant attention as a highly promising alternative to traditional Ni-cermet anode supported cells.[4,5] In this configuration, the same material is employed for both the cathode and anode, substantially reducing fabrication time and costs, as only a single step is required to assemble both electrodes on the electrolyte. Additionally, SSOCs offer the potential benefit of mitigating sulphur and carbon deposits in the fuel electrode through controlled gas flow alternation, thereby extending the lifetime of the cell.[6]

Several electrode materials have been proposed for SSOCs, such as $La_{0.75}Sr_{0.25}Cr_{0.5}Mn_{0.5}O_{3-\delta}$,[7] $PrBaMn_2O_{5+\delta}$,[8] $Sr_2Fe_{1.5}Mo_{0.5}O_{6-\delta}$,[9] or $La_{0.3}Sr_{0.7}Fe_{0.9}Ti_{0.1}O_{3-\delta}$.[10] While these materials have demonstrated high efficiency working as fuel electrode, their performance as oxygen electrode is relatively poor. On this way, lanthanum ferrite-based perovskites are one of the most promising candidates due to their remarkable results in both oxidizing and reducing conditions, along with their excellent chemical stability through appropriate doping strategies.[11]

In this context, multiple substitution strategies have been explored to enhance the electrochemical properties and improve the redox stability of the $La_{1-x}Sr_xFeO_{3-\delta}$ perovskite by incorporating elements such as Cr^{3+}, Mn^{3+}, Ti^{4+}, Nb^{5+} or Mo^{6+}.[12–16] Among these, titanium-doped ferrites have demonstrated excellent redox stability and remarkable electrochemical performance in both air and fuel atmosphere.[17,18] Moreover, to further enhance the electrochemical performance, highly active elements have been introduced into the B-site of $La_{1-x}Sr_xFeO_{3-\delta}$, *i.e.,* Ru,[19] Pd,[20] Pt [21,22] or Ni,[19,23], significantly enhancing the efficiency for fuel oxidation through nanoparticle exsolution. The in-situ exsolution from the perovskite lattice results in a homogeneous distribution of well-anchored nanoparticles, preventing agglomeration and thus extending the active sites for electrochemical reactions.[24] However, in most of the cases, either solid-state reaction or precursor routes have been used to synthesize

the aforementioned materials, requiring relatively high temperatures for achieving phase formation and good adhesion to the electrolyte when using screen-printing deposition. These high-temperature calcinations lead to a large ceramic grain size that negatively affects the electrochemical performance of the electrodes, particularly in the oxygen reduction reaction (ORR) due to its sluggish kinetics.[25]

For this reason, the synergy of both doping and microstructural strategies becomes crucial for the development of highly efficient electrode materials.[26] The triple phase boundary (TPB) sites, where electrochemical reactions occur through interactions between ions, electrons and reactants, can be extended by designing different electrode architectures with enhanced porosity and active surface area. In this context, several approaches have been proposed to improve the electrode efficiency, including infiltration into a porous backbone,[27] nanocomposite materials[28] or the incorporation of thin active layers.[29] However, these preparation methods often involve multiple steps and/or lengthy processes, followed by relatively high calcination temperatures for deposition and sintering.

Alternatively, spray-pyrolysis has proven to be a cost effective and versatile method for producing thin electrodes with different morphologies over large areas by tailoring the deposition conditions, varying from porous to dense layers.[30] Hence, this approach offers a promising solution to overcome the limitations of conventional methods, as it allows for the fabrication of advanced electrode architectures with improved properties, including enhanced porosity and active surface area.

In this study, symmetrical electrodes of $(La_{0.8}Sr_{0.2})_{0.95}Fe_{1-x}Ti_xO_{3-\delta}$-$Ce_{0.9}Gd_{0.1}O_{1.95}$ ($LSFT_x$, x=0.2 and 0.4) with advanced architectures are investigated. To enhance the redox stability of $(La,Sr)FeO_3$-based electrodes, a Ti-doping strategy was employed. A Ti content above x=0.2 is essential to achieve the desired stability in an H_2 atmosphere, as corroborated by previous studies.[31,32] The electrodes were prepared by freeze-dried powder precursors (FD), followed by screen-printing deposition or alternatively, by employing spray-pyrolysis deposition in a single-step process at reduced temperature. A Ni-doping strategy was also implemented to further enhance the electrode performance for fuel oxidation. In order to tailor the electrode microstructure and study its influence on the electrochemical properties, different strategies were investigated: (i) traditional screen-printed composite powder electrodes, (ii) traditional composite powder electrodes with exsolved Ni nanoparticles, (iii) nanocomposite layers deposited directly onto the electrolyte, (iv) infiltrated electrodes and (v) infiltrated

electrodes with exsolved Ni nanoparticles (Figure 1). A comprehensive structural, morphological and electrical characterization have been carried out by X-ray diffraction, electron microscopy and impedance spectroscopy. In order to understand the electrode mechanisms for the oxygen reduction reaction or hydrogen oxidation reaction, the electrochemical properties have been investigated as function of the temperature, oxygen partial pressure and applied dc bias. Finally, the most promising symmetrical electrode candidates were tested in electrolyte-supported cell configuration in real SOFC conditions.

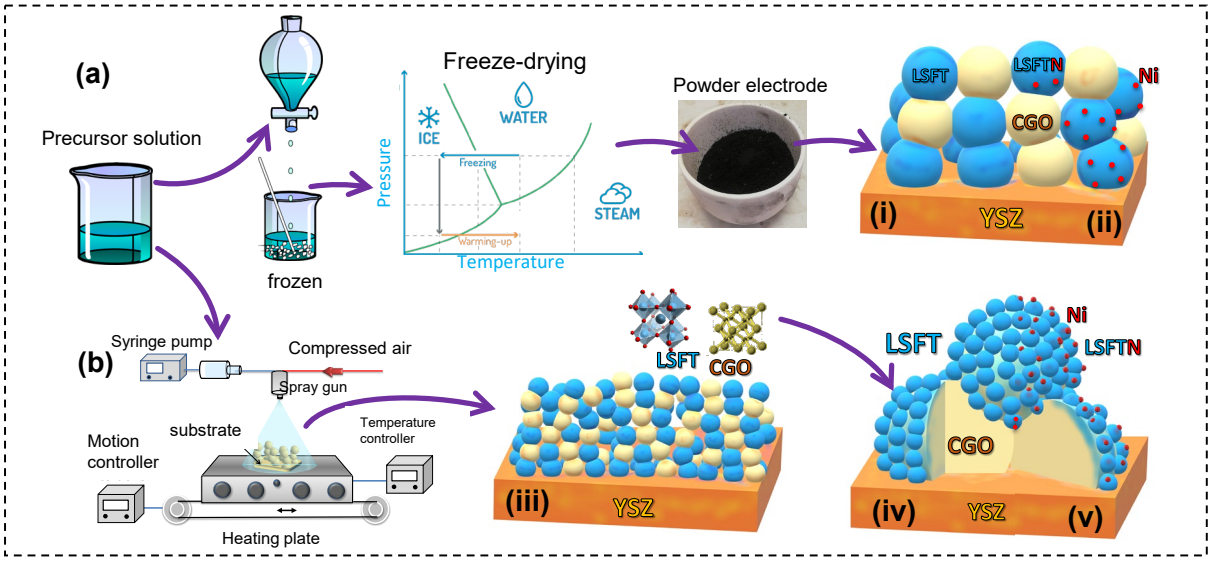

Figure 1. Schematic representation of the different microstructural strategies studied in this work by (a) freeze-drying precursor method (FD) to obtain powder electrodes and (b) spray-pyrolysis deposition to prepared advanced electrode architectures directly onto the electrolyte: (i) traditional composite powder and (ii) composite powder with exsolved Ni nanoparticles, (iii) nanocomposite layer, (iv) infiltrated electrode and (v) infiltrated electrode with exsolved Ni nanoparticles.

2. Experimental

2.1. Materials preparation

$Zr_{0.84}Y_{0.16}O_{1.92}$ (YSZ, Tosoh) and $La_{0.9}Sr_{0.1}Ga_{0.8}Mg_{0.2}O_{3-\delta}$ (LSGM, Kceracell) pellets were prepared by compacting 0.30 g of commercial powders into disks of 10 mm and 1 mm of diameter and thickness, respectively. The pellets were subsequently sintered at 1400 ºC for 4 h in air to obtain fully dense electrolytes. In order to create a porous backbone layer, the pellets were symmetrically screen-printed using a slurry composed of $Ce_{0.9}Gd_{0.1}O_{1.95}$ (CGO, Rhodia) powders mixed with Decoflux (Zschimmer and Schwarz), followed by sintering at 1200 ºC for 1 h.

The electrode powder materials, $(La_{0.8}Sr_{0.2})_{0.95}Fe_{0.8}Ti_{0.2}O_{3-\delta}$ ($LSFT_{0.2}$-FD), $(La_{0.8}Sr_{0.2})_{0.95}Fe_{0.6}Ti_{0.4}O_{3-\delta}$ ($LSFT_{0.4}$-FD), and a composite consisting of 50 wt.%

$(La_{0.8}Sr_{0.2})_{0.95}Fe_{0.8}Ti_{0.2}O_{3-\delta}$-$Ce_{0.9}Gd_{0.1}O_{1.95}$ ($50LSFT_{0.2}$-FD), were prepared using the freeze-drying (FD) precursor method (Figure 1a, Table S1). Precursor cation solutions were obtained by dissolving stoichiometric amounts $La(NO_3)_3 \cdot 6H_2O$, $Sr(NO_3)_2$, $Fe(NO_3)_3 \cdot 9H_2O$ and $Ti[OCH(CH_3)_2]_4$ in Milli-Q water to achieve a cation concentration of 0.5 mol L^{-1}. Ethylenediamine-tetraacetic acid (EDTA) was used as complexing agent in a 1:4 ligand:metal molar ratio. In the case of the composite electrode, $Ce(NO_3)_3 \cdot 6H_2O$ and $Gd(NO_3)_3 \cdot 6H_2O$ were also added to obtain a single precursor solution containing all elements in stoichiometric amounts ($50LSFT_{0.2}$-FD). It is important to note that the electrodes were prepared with A-site deficiency to minimize the possible segregation of Sr-based compounds. The precursor solutions were frozen in liquid nitrogen and then dehydrated by vacuum sublimation in a Coolsafe freeze-dryer. The dried precursors were initially calcined at 300 ºC to pyrolyze the organic matter and then further calcined at 800 ºC for 1 h to achieve crystallization. Composite powders, obtained by (a) physically mixing $LSFT_{0.2}$ and CGO in a 50 wt.% ratio ($50LSFT_{0.2}$-PM) and (b) using the co-sintered powders ($50LSFT_{0.2}$-FD), were screen-printed onto the electrolyte and sintered at 1100 ºC for 1 h to achieve an adequate adhesion.

Nanostructured electrodes with the same composition were also prepared by spray-pyrolysis deposition by using different approaches. Detailed information about the spray-pyrolysis system can be found elsewhere.[33] Initially, the $LSFT_{0.2}$-CGO ($50LSFT_{0.2}$) nanocomposite layer was directly deposited onto the electrolyte at 325 ºC by preparing a similar precursor solution containing the corresponding cations of both phases with a concentration 0.02 M, followed by calcination at 800 ºC in air (Figure 1b (iii)). It is worth mentioning that 325 ºC was identified as the optimal deposition temperature for obtaining homogeneous and porous layers with improved adhesion to the electrolyte.[33] In an alternative approach, $LSFT_{0.2}$ and $LSFT_{0.4}$ electrodes were infiltrated onto the porous CGO backbones at 325 ºC for 1 h using the spray-pyrolysis deposition, designated as $LSFT_{0.2}$-Inf and $LSFT_{0.4}$-Inf, respectively, (Figure 1b (iv)).

Additionally, a Ni-containing phase, $(La_{0.8}Sr_{0.2})_{0.95}(Fe_{0.8}Ti_{0.2})_{0.9}Ni_{0.1}O_{3-\delta}$ (LSFTN), was prepared to promote the Ni-exsolution in reducing conditions and improve the hydrogen oxidation reaction (HOR) kinetics. LSFTN composition was synthesized as powder the through the freeze-drying method (LSFTN-FD) (Figure 1a (ii)) and as an infiltrated layer within a porous CGO backbone using spray-pyrolysis (LSFTN-Inf) (Figure 1b (v)), following the same conditions as previously described.

2.2. Structural, microstructural and electrical characterization

The structure was characterized using X-ray powder diffraction (XRD) with an Empyrean PANalytical diffractometer equipped with CuK$\alpha_{1,2}$ radiation in the 2θ range of 20-80º with a step size of 0.013º and a time per step of 1.58 s with a PIXcel detector. The diffraction patterns were analyzed and fitted with the HighScore Plus and GSAS suite software.[34,35]

The morphology of the different electrode architectures was studied by scanning electron microscopy (SEM) in a FEI-SEM (Helios Nanolab 650). The composition and grain size of the nanocomposite electrodes were characterized using High-Angle Annular Dark-Field Scanning Transmission Electron Microscopy (HAADF-STEM) and HR-TEM in a Talos F200X, FEI.

X-ray photoelectron spectroscopy (XPS) measurements were carried out on a Physical Electronics spectrometer (PHI 5700) with Mg K_α source (300 W, 15 kV and 1253.6 eV). High-resolution spectra were recorded with a concentric hemispherical analyzer operating in constant pass energy mode at 29.35 eV, using a 720 μm diameter analysis area at the optimum equipment take-off angle of 45°. The data were analyzed and deconvoluted with the Multipak-V9.3 software package.

The electrochemical properties were tested by impedance spectroscopy in a Solartron 1260 FRA, employing a frequency range of 0.01-10^6 Hz and an AC amplitude of 100 mV. To obtain a current collector layer, Pt-ink (METALOR® 6082) was painted on both electrodes and then calcined at 750 ºC for 15 min. The impedance spectra were also collected as a function of the oxygen partial pressure (pO_2) from 0.21 to 10^{-2} atm using an electrochemical cell equipped with YSZ oxygen sensor and pump.[33] The system was flushed with a gas mixture of O_2 and N_2 at 700 ºC for 1 h, and the cells were equilibrated at each oxygen partial pressure for at least 30 min before acquiring the impedance spectra. The impedance spectra were analyzed by distribution of relaxation times (DRT) using DRTtools software.[36] In addition, the electrode performance was studied under a dc bias by using a three-probe configuration. A 0.20 cm^2 counter and working electrode were symmetrically deposited onto a 18 mm diameter YSZ pellet, with an external Pt ring surrounding the working electrode, which served as a reference electrode.[33] The applied dc bias ranged from 0 to ±0.4 V at different temperatures between 700-500 ºC to study the influence of the applied current on the electrode performance.

The overall conductivity of the samples was determined by Van der Pauw four-probe method under air and 5% H_2-Ar atmosphere on cooling at different temperatures from 750 to 400 ºC.[37] To obtain dense pellets, the powders obtained by the freeze-drying method were pressed into pellets with diameter of 13 mm and thickness of 1 mm. The pellets were subsequently sintered at 1400 ºC for 1 h in the case of $LSFT_{0.2}$-FD and $LSFT_{0.4}$-FD samples, and at 1300 ºC for 1 h for $50LSFT_{0.2}$-FD sample, reaching relative densities above 95%.

For the fuel cell tests with an electrolyte-supported configuration, dense 300 μm thin pellets of $La_{0.9}Sr_{0.1}Ga_{0.8}Mg_{0.2}O_{3-\delta}$ (LSGM, Kceracell) were prepared by compacting the commercial powders into disks with a 13 mm diameter and then sintered at 1400 ºC for 1 h in air. The electrodes were symmetrically deposited on the LSGM electrolyte using either the spray-pyrolysis or screen-printing method, covering a circular area of 0.20 cm^2 through a shadow mask as described earlier. To seal the single cell to the electrochemical setup, a glass-ceramic material (Ceramabond 668, Aremco) was employed. Both current-voltage characteristics and impedance spectra were collected at different temperatures ranging from 800 to 650 ºC. The measurements were conducted using a Zahner XC electrochemical workstation with static air as the oxidant and humidified H_2 (3% H_2O) as the fuel.

3. Results and discussion

3.1. Microstructure of the different electrode architectures

Figure 2 compares the cross-sectional SEM images of the different electrode architectures investigated in this work. The traditional composite electrode, labelled as $50LSFT_{0.2}$-PM, prepared by mixing $LSFT_{0.2}$ and CGO powders, followed by screen-printing and sintered at 1100 ºC for 2 h, exhibits high porosity with an average particle size around 250 nm of diameter and an electrode thickness of 10 μm (Figure 2a,b). In this case, the high annealing temperature required to ensure adequate adhesion to the electrolyte resulted in a relatively large grain growth, which is expected to have adverse effects on the electrochemical properties of this electrode. The sintering temperature of the electrodes has a significant impact on their microstructure and, consequently, their performance. Numerous studies have consistently reported that a gradual increase in grain size and a reduction in electrode porosity negatively affect the electrochemical properties of the electrodes.[38–40]

The nanocomposite electrode ($50LSFT_{0.2}$), which was directly deposited onto the electrolyte, exhibits a considerably reduced particle size (~30 nm) after annealing at 800 ºC, in contrast to the corresponding electrode prepared by screen-printing deposition (Figure 2c,d).

This notable decrease in the particle size can be attributed to the co-sintering of both $LSFT_{0.2}$ and CGO that ensures a nanoscale contact between the two phases.[37] In the case of the powder electrodes prepared through freeze-drying (FD) and screen-printing deposition, the reduced particle size is attributed to the co-sintering of both $LSFT_{0.2}$ and CGO phases. This phenomenon is a result of cation diffusion limitations at the grain-boundary region due to the presence of two immiscible phases.[41,42] Regarding the electrodes prepared by spray-pyrolysis, both the co-sintering and reduced fabrication temperature play significant roles. The direct deposition of these electrodes onto the electrolyte using spray-pyrolysis ensures excellent adhesion at a reduced temperature of 800 ºC, in contrast to the higher sintering temperature required for traditionally screen-printed electrodes (1100 ºC).

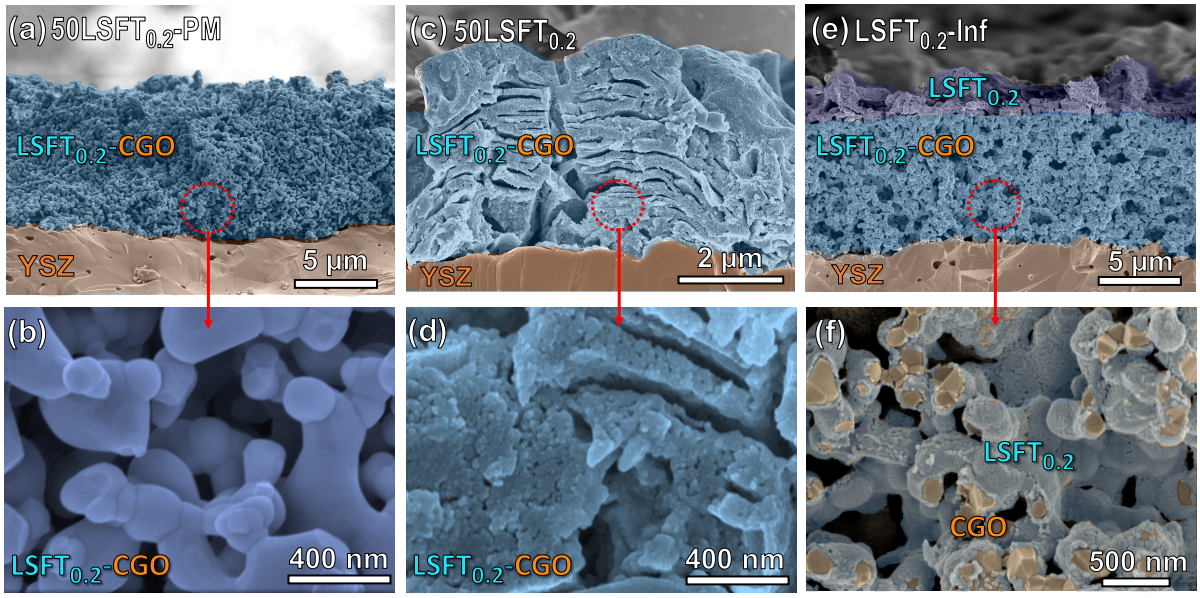

Figure 2. Cross-sectional SEM images at different magnification of the different electrode architectures: (a,b) screen-printed $50LSFT_{0.2}$-PM; (c,d) $50LSFT_{0.2}$ nanocomposite layer and (e,f) $LSFT_{0.2}$-Inf deposited by spray-pyrolysis. The images are not given at the same magnification due to the different particle size among the electrodes.

The electrodes infiltrated into a CGO backbone by spray-pyrolysis ($LSFT_{0.2}$-Inf) show a double-layer architecture (Figure 2e,f). The inner porous backbone with a thickness of 10 µm is fully coated with a layer of $LSFT_{0.2}$ nanoparticles (~50 nm in diameter), which significantly extends the TPB sites for the electrocatalytic reactions. Additionally, a superficial porous layer of $LSFT_{0.2}$ nanoparticles is visible on top of the CGO backbone, which can be attributed to the non-infiltrated excess material during the spray-pyrolysis deposition. This layer, which is approximately 1 µm thick, primarily acts as a current collector due to its higher electronic conductivity and lower porosity when compared to the inner layer.

To improve the performance of the fuel electrode, a Ni-containing phase, $(La_{0.8}Sr_{0.2})_{0.95}(Fe_{0.8}Ti_{0.2})_{0.9}Ni_{0.1}O_{3-\delta}$ (LSFTN), was also considered to promote the Ni-exsolution under reducing conditions. The LSFTN-FD sample, prepared by freeze-drying, was reduced at 750 ºC for 12 h in 5% H_2-Ar atmosphere to study the Ni exsolution process (Figure 3). SEM image of the LSFTN-FD after reduction reveals a homogeneous distribution of exsolved Ni nanoparticles of ~15 nm diameter on the electrode surface (Figure 3a). The HAADF-STEM-EDS images further confirm the presence of Ni nanoparticles (Figure 3b-f). Interestingly, the exsolution process did not induce significant morphological changes of the electrodes, nor did it result in the segregation of secondary phases. Similar results were found for the LSFTN-Inf sample prepared by spray-pyrolysis (Figure S1, Supplementary Information). It is worth that in this work, the electrodes were prepared with slight A-site deficiency and a low Ni-doping content (10 mol% in B-site) to facilitate the exsolution of Ni nanoparticles in H_2 atmosphere without inducing any phase transitions or additional secondary phases.[43,44] In contrast, ferrite-based electrodes with higher Ni-dopant contents and without Ti-doping, such as $PrNi_{0.4}Fe_{0.6}O_{3-\delta}$ and $Pr_{0.6}Sr_{0.4}Fe_{0.7}Ni_{0.2}Mo_{0.1}O_{3-\delta}$,[45,46] have shown phase decomposition in a reducing atmosphere, leading to substantial morphological changes in the electrodes. The lattice d-spacing observed in the HRTEM image of the Ni-exsolved nanoparticle is similar to that expected for Ni metal (Figure 3g). In general, the Ni exsolution mechanism in 5% H_2-Ar is attributed to nickel oxide migration to the surface, followed by reduction to Ni-metal, which subsequently grows through particle nucleation.[43]

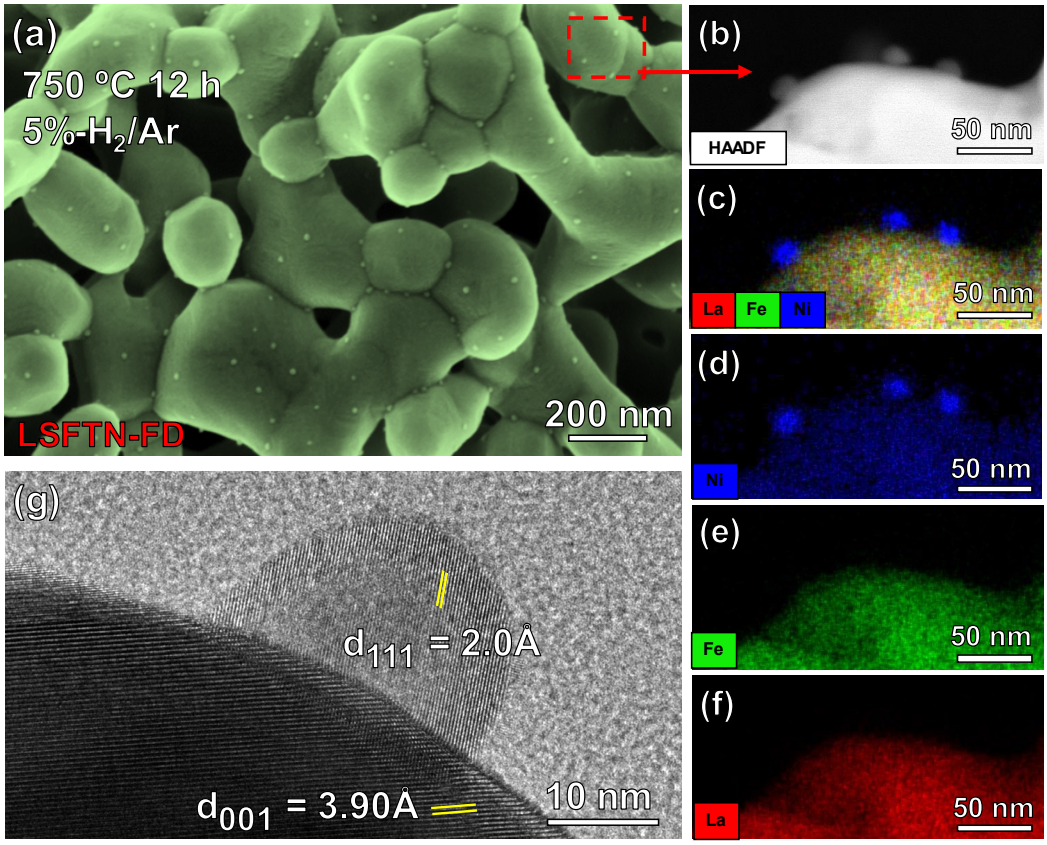

Figure 3. (a) SEM image of LSFTN-FD electrode after reduction at 750 ºC for 12 h in 5% H_2-Ar. (b) HAADF-STEM image and (c-f) EDS mapping confirming the presence of Ni nanoparticles on the electrode surface. (g) HRTEM image showing the interatomic distances of the LSFT perovskite lattice and the Ni metal nanoparticle.

3.2. Structural characterization

XRD characterization of the $(La_{0.8}Sr_{0.2})_{0.95}Fe_{1-x}Ti_xO_{3-\delta}$ (x=0.2, 0.4; $LSFT_x$) electrodes with different architectures and synthetic strategies was performed to gain insights into their crystal structure. XRD patterns of $LSFT_{0.2}$-FD powders, as a representative example, after calcination at different temperatures in air and H_2 are shown in Figure S2. Regardless of the Ti-content, the XRD analysis revealed the formation of an orthorhombic phase (s.g. *Pbnm*), demonstrating exceptional redox stability at elevated annealing temperatures (Figure S3).

The cell volume, obtained by the Rietveld method, decreases with increasing Ti-content from 241.436 (2) to 240.768 (2) $Å^3$ for $LSFT_{0.2}$-FD and $LSFT_{0.4}$-FD, respectively (Table S2, Figure S3). This reduction in cell volume can be attributed to the lower ionic radii of Ti^{4+} (0.605 Å) compared to Fe^{3+} (0.645 Å) when both ions are present in an octahedral environment. These findings are consistent with previous reports on the $La_{0.6}Sr_{0.4}Fe_{1-x}Ti_xO_{3-\delta}$ (x= 0.1 and 0.3) series.[47]

After a calcination at 1400 ºC for 1 h, the cell volume increases, 242.102 (3) and 241.915 (2) $Å^3$ for $LSFT_{0.2}$-FD and $LSFT_{0.4}$-FD, respectively. This increase in cell volume can be attributed to changes in the oxidation states of iron when the temperature is increased, leading to changes in the lattice oxygen stoichiometry (Table S2).[47] Afterwards, the powders were reduced at 750 ºC for 12 h in 5% H_2-Ar atmosphere. The cell volumes of $LSFT_{0.2}$-FD and $LSFT_{0.4}$-FD slightly increase up to 242.247 (3) and 242.771 (2) $Å^3$, respectively, due to the partial reduction of iron and titanium cations in the lattice. The more pronounced increase in the cell volume of $LSFT_{0.4}$ can be ascribed to its higher titanium content, which undergoes a reduction from Ti^{4+} (0.605 Å) to Ti^{3+} (0.670 Å) under reducing conditions. Interestingly, Ni-doped LSFT (LSFTN-FD) exhibits a cell volume very similar to the pristine sample in both air (240.408 (2) $Å^3$) and hydrogen atmosphere (241.274 (3) $Å^3$), suggesting that the Ni^{2+} incorporation (0.645 Å) into the B-site of the perovskite and the subsequent exsolution process do not induce significant structural change in the pristine sample (Figure S2 and Table S2).

Figure 4a displays the XRD patterns of the $50LSFT_{0.2}$-FD nanocomposite prepared using the freeze-drying method via co-sintering. Interestingly, the crystallite size (d) obtained by the Scherrer's equation at 800 ºC was as low as 19.2 and 11.5 nm for $LSFT_{0.2}$ and CGO phases, respectively, which are notably lower than that observed for the $LSFT_{0.2}$ single phase at the same temperature (37.4 nm) (Table S2). These findings confirm the effective suppression of grain growth due to the intimate nanoscale mixture of two immiscible phases, which limits the cation diffusion at the grain boundaries.[41,42] Upon increasing the temperature to 1000 ºC, the crystallize size slightly increases to 41.2 for $LSFT_{0.2}$ and 35.4 nm for CGO phases, without the presence of any secondary phases.

The $50LSFT_{0.2}$-FD nanocomposite displays cell volumes of 240.762(2) for $LSFT_{0.2}$ and 162.067(2) $Å^3$ for the CGO phase (Table S2), which are quite similar to those observed in the individual materials. HAADF-STEM-EDS images of the $50LSFT_{0.2}$-FD electrode calcined at 1100 ºC confirmed the formation of both $LSFT_{0.2}$ and CGO phases without the presence of secondary phases (Figure S4), as observed by XRD. However, the particle size is relatively large, ~ 100 nm, due to the high sintering temperature employed. The slight changes in the cell volume may be attributed to minor cation exchange between $LSFT_{0.2}$ and CGO phases during the co-sintering process. For instance, a minor incorporation of La^{3+} (1.16 Å) into the CGO lattice with higher ionic radii, Ce^{4+} (0.97 Å), could explain the observed increase of the lattice cell volume for the CGO component.[48] However, despite these slight changes, the phase

fraction obtained by the Rietveld refinement remains consistent with the nominal one. Moreover, this limited cation exchange between both phases is not expected to have a detrimental impact on the electrode performance. For example, Ce-doped (La,Sr)FeO_3 has shown improved properties for HOR.[49] In the case of the nanocomposite material deposited directly onto YSZ electrolyte (50LSFT$_{0.2}$), similar lattice parameters and crystallite size are obtained (Figure 4b and Table S2). HAADF-STEM-EDS and HR-TEM images of the nanocomposite 50LSFT$_{0.2}$ electrode are displayed in Figure 4d-f. The EDS mapping reveals that the nanocomposite layer consists of nanoparticles of 30 nm diameter, confirming the intimate mixture of the LSFT$_{0.2}$ and CGO phases, which ensures a great extension of the TPB length for electrochemical reactions. The crystal structure of both phases is further confirmed by the d_{hkl} interplanar distances, consistent with the XRD data (Figure 4f). It is worth mentioning that the crystallize size obtained from the Scherrer´s equation is comparable to that observed by SEM and TEM. For instance, in the case of 50LSFT$_{0.2}$ calcined at 800 ºC, an average crystalline size of 18.6 nm is obtained, while the average particle size is ~30 nm.

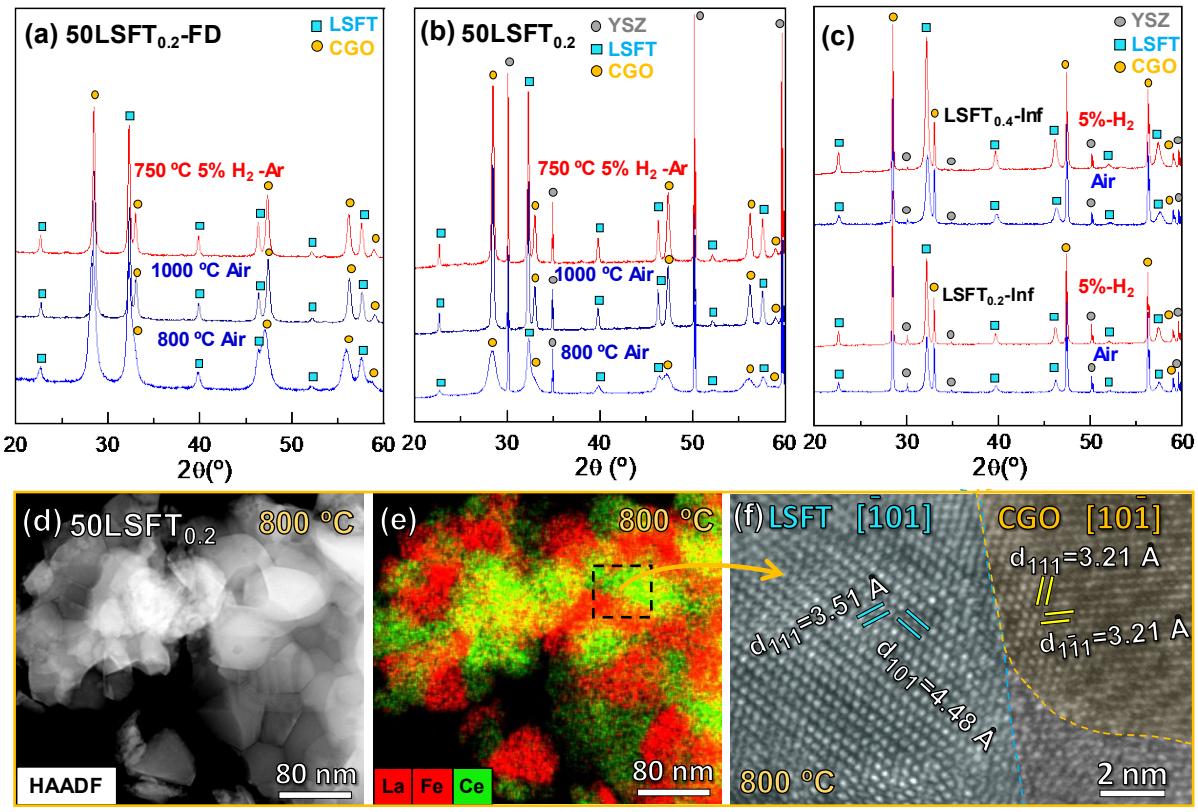

Figure 4. XRD patterns after a calcination in air at different temperatures between 800-1000 ºC and 750 ºC in 5% H_2-Ar for 12 h of (a) 50LSFT$_{0.2}$-FD powders; (b) 50LSFT$_{0.2}$ layer; and (c) LSFT$_{0.2}$-Inf and LSFT$_{0.4}$-Inf electrodes deposited into CGO backbone and YSZ electrolyte. (d) HAADF-STEM image and (e) EDS mapping of 50LSFT$_{0.2}$ after calcination at 800 °C in air. (f) HRTEM image showing the interatomic distances of the LSFT$_{0.2}$ and CGO phases.

The infiltrated samples, $LSFT_{0.2}$-Inf and $LSFT_{0.4}$-Inf, also exhibit a perovskite-type structure at 800 ºC, similar to that observed for the powder electrodes prepared by freeze-drying (Figure 4c). The cell volumes of $LSFT_{0.2}$-Inf and $LSFT_{0.4}$-Inf at 800 ºC, 241.510 (2) and 240.751 (1) $Å^3$, respectively, closely match those observed in the corresponding powders. Importantly, additional diffraction peaks associated with secondary phases are not detected after the stability test in reducing conditions at 750 ºC in 5% H_2-Ar atmosphere for 12 for all compositions, confirming the excellent redox stability of the materials.

3.3. Electrochemical characterization

The total conductivity of the samples was determined by the Van der Pauw method in air and 5% H_2-Ar, as well as a function of the oxygen partial pressure (pO_2). Figures 5a,b show the SEM images of $LSFT_{0.2}$-FD and $50LSFT_{0.2}$-FD pellets sintered at 1300 and 1400 ºC for 1 h, which represent the optimal temperatures for achieving relative densities above 95%.

Remarkably, the $50LSFT_{0.2}$-FD sample obtained from the thermal co-synthesis composite method shows improved densification at lower temperatures, resulting in a smaller grain size (0.5 μm), with an excellent homogeneous distribution of both $LSFT_{0.2}$ and CGO phases (Figure 5b). It is worth noting that clean grain boundaries are observed without the presence of reaction products or impurities, even at temperatures as high as 1300 ºC, confirming the great stability of these electrodes. In the case of the $LSFT_{0.4}$-FD, the average grain size is lower (~0.6 μm) compared to that observed for $LSFT_{0.2}$-FD (~1.9 μm), and the EDS mapping reveals a homogenous cation distribution for both samples (Figure S5-6).

The electrical conductivity of the dense pellets, measured in air and 5% H_2 as a function of the temperature, is shown in Figure 5d. In air atmosphere, the conductivity decreases with increasing Ti-doping, reaching values of 0.47 and 0.003 S cm^{-1} at 700 ºC for $LSFT_{0.2}$-FD and $LSFT_{0.4}$-FD, respectively. This decrease in conductivity with increasing Ti-content is possibly attributed to the stable oxidation state of Ti^{4+} in atmospheric air, which hinders the movement of the electronic charge carriers.[50] The $50LSFT_{0.2}$-FD composite electrode exhibits relatively low conductivity values at 700 ºC (0.006 S cm^{-1}) in air, mainly due to the lower electrical conductivity of CGO.[51]

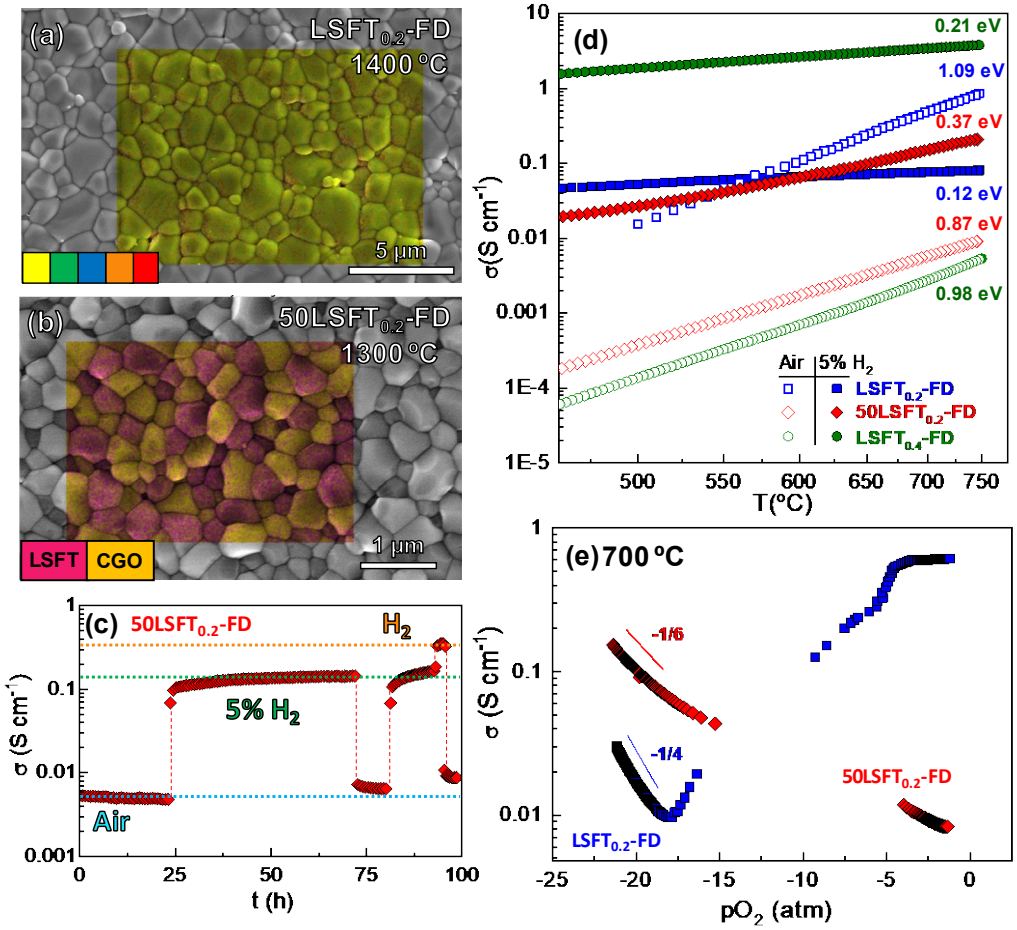

Figure 5. SEM images of (a) $LSFT_{0.2}$-FD and (b) $50LSFT_{0.2}$-FD composite dense pellets. The EDS mapping in (a,b) shows the phase distribution. (c) Variation of the conductivity of the $50LSFT_{0.2}$-FD sample after several oxidation/reduction cycles in air, 5% H_2-Ar and H_2 at 700 ºC. (d) Total conductivity in air and 5% H_2-Ar of the different electrode compositions as a function of the temperature. (e) Total conductivity as a function of the oxygen partial pressure (pO_2) of $LSFT_{0.2}$-FD and $50LSFT_{0.2}$-FD at 700 ºC.

In 5% H_2-Ar, the conductivity of $LSFT_{0.2}$-FD decreases to 0.08 S cm^{-1} at 700 ºC, primarily as a result of the reduction of iron with the consequent decrease of charge carriers. A decrease in conductivity under reducing conditions have been widely observed for ferrite-based electrodes, such as $La_{0.3}Sr_{0.7}Fe_{0.9}Ti_{0.1}O_{3-\delta}$, $La_{0.7}Sr_{0.3}Ti_{0.1}Fe_{0.6}Ni_{0.3}O_{3-\delta}$ and $La_{0.4}Sr_{0.6}Fe_{0.6}Ti_{0.4}O_{3-\delta}$ [10,49,56]. [10,50,52] This can be attributed to the reduction of Fe^{4+} (the electronic hole charge carriers) to lower oxidation states, thereby reducing the conductivity. XPS results revealed that Fe^{2+} is the dominant oxidation state of iron after reduction in 5% H_2-Ar (Figure S7).

In contrast, the conductivity of $LSFT_{0.4}$-FD increases up to 3.45 S cm^{-1} at 700 ºC due to the partial reduction of Ti^{4+} to Ti^{3+},[53] which enhances the availability of charge carriers and leads to a significant increase in electronic conductivity. The conductivity of $50LSFT_{0.2}$-FD

composite increases to 0.15 S cm^{-1} at 700 ºC, primarily due to the partial reduction of Ce^{4+} to Ce^{3+}, thus improving the n-type electronic conductivity.

The activation energy (E_a) of the conductivity in air is quite similar for all samples, ranging from 0.89 to 1.09 eV, which is indicative of predominant ionic conduction. In 5% H_2-Ar atmosphere, the activation energy decreases significantly (0.12-0.37 eV) due to the predominant electronic conduction. In the case of the composite electrode (50LSF$T_{0.2}$-FD), the activation energy in reducing conditions (0.37 eV) is notably higher compared to that observed for the single composition (LSF$T_{0.2}$-FD) with a value of 0.12 eV. This difference in activation energy can be attributed to the presence of CGO, which has dominant oxide-ion conductivity within the composite material, thereby affecting its electronic conduction properties.

To investigate the redox stability of 50LSF$T_{0.2}$-FD, the electrical conductivity was measured in consecutive oxidation/reduction cycles at 700 ºC, and the results showed good cyclability without any significant drops in conductivity (Figure 5c). Remarkably, the reduction/oxidation processes took less than 1 h, despite the high relative density of the samples (96 %). An interesting observation was that the conductivity values under reducing condition raised from 0.15 to 0.35 S cm^{-1} when the gas was shifted from 5% H_2-Ar to 100% H_2, respectively. This enhancement can be attributed to the higher charge carrier concentration at lower pO_2 values.

The conductivity was determined as a function of the oxygen partial pressure (pO_2) to elucidate the nature of the charge carriers (Figure 5e). For LSF$T_{0.2}$-FD, a predominant n-type conductivity was observed at very low pO_2, showing a $(pO_2)^{-1/4}$ dependence. The conductivity then reaches a minimum value at $pO_2 \sim 10^{-17}$ atm, indicating an n-p-type electronic transition regime. Above this pO_2, the conductivity increases with a $(pO_2)^{1/4}$ dependence, attributed to a p-type contribution with hole-conduction, as predicted in the defect chemistry model of $La_{0.9}Sr_{0.1}FeO_{3-\delta}$ and $La_{0.75}Sr_{0.25}FeO_{3-\delta}$ in previous studies.[54,55] In the case of 50LSF$T_{0.2}$-FD, a $(pO_2)^{-1/6}$ dependence is observed at low pO_2, which is likely due to the significant n-type contribution from the CGO phase, which experiences a drastic reduction of Ce^{4+} to Ce^{3+} at low pO_2, leading to the formation of a large concentration of extrinsic vacancies, similar to what is observed in $Ce_{0.8}Sm_{0.2}O_{1.9}$.[56]

In general, the conductivity values obtained in air in this work are lower compared to some related compositions reported in the literature, such as $La_{0.5}Sr_{0.5}Fe_{0.9}Ti_{0.1}O_{3-\delta}$ (90 S cm^{-1}

at 600 ºC) [57] and $La_{0.7}Sr_{0.3}Fe_{0.6}Ti_{0.1}Ni_{0.3}O_{3-\delta}$ (318 S cm^{-1} at 700 ºC).[52] These differences in conductivity can be attributed to several factors, including variations in crystal structures (ranging from orthorhombic to cubic) and the smaller titanium content in the B-site of the perovskite. Additionally, the La/Sr ratio in the A-site has shown to play a significant role in determining the conducting properties, with compositions having higher Sr-contents typically exhibiting higher electrical conductivity.[50] Despite the lower concentration of Fe^{4+} ions (electronic charge carriers) and the smaller amount of oxygen vacancies in compositions with higher lanthanum content, these materials exhibit improved redox stability for potential application in symmetrical fuel cells.[50] On the other hand, it is noteworthy that the conductivity values in reducing conditions are comparable to those reported previously for similar compositions like $La_{0.4}Sr_{0.6}Fe_{0.6}Ti_{0.4}O_{3-\delta}$ (0.5 S cm^{-1})[50] and $La_{0.3}Sr_{0.7}Fe_{0.9}Ti_{0.1}O_{3-\delta}$ (0.25 S cm^{-1})[10] at 600 ºC.

XPS analysis was performed to study the chemical composition and cation oxidation state of the elements in the powder materials of $LSFT_{0.2}$-FD (Figure S7) and $LSFT_{0.4}$-FD (Figure S8) after annealing under oxidizing and reducing conditions. In the case of $LSFT_{0.2}$-FD, the deconvolution of the Fe $2p_{3/2}$ core level shows three different contributions (Fe^{2+}, Fe^{3+} and Fe^{4+}) with corresponding binding energies of 710.1, 711.9 and 716.8 eV, respectively. Similar results have been observed previously for related compositions such as $LaFeO_3$ and $La_{0.6}Sr_{0.4}Fe_{0.95}Pd_{0.05}O_{3-\delta}$.[20,58] In addition to the main peaks, a shake-up satellite peak from the Fe $2p_{3/2}$ region is also observed. Upon reduction, the area of the Fe^{2+} band increases, confirming a partial reduction of iron, as expected. These findings are in accordance with the decrease in conductivity values in $LSFT_{0.2}$-FD, attributed to the partial reduction of $Fe^{3+/4+}$ to a lower oxidation state.

The same trend was observed for $LSFT_{0.4}$-FD (Figure S8), indicating a consistent behavior across both materials. Notably, no significant changes were detected for the other elements after reduction, highlighting the high redox stability of the materials (Figure S7-8). Furthermore, it is worth mentioning that the presence of Ti^{3+} in the Ti2p core level could not be identified, suggesting that the Ti^{3+} concentration is below the XPS detection limits (Figure S7-8), in line with previous reports.[59]

Impedance spectra for the different compositions and electrode architectures were measured in a symmetrical cell configuration at open circuit voltage under both oxidizing and reducing conditions (Figure 6). To facilitate a better comparison of each electrode contribution,

the ohmic resistance attributed to the electrolyte was subtracted. The screen-printed composite electrodes, 50LSFT$_{0.2}$-PM and 50LSFT$_{0.4}$-PM, exhibit R_p values of 1.19 and 8.84 Ω cm^2, respectively, at 700 ºC in air. As expected, the electrode with higher Ti-content, LSFT$_{0.4}$-FD, exhibits poorer electrochemical activity, which can be attributed to its low electrical conductivity in air. Similar findings have also been observed in the SrFe$_{1-x}$Ti$_x$O$_{3-\delta}$ ($0 < x \leq 0.5$) series.[60]

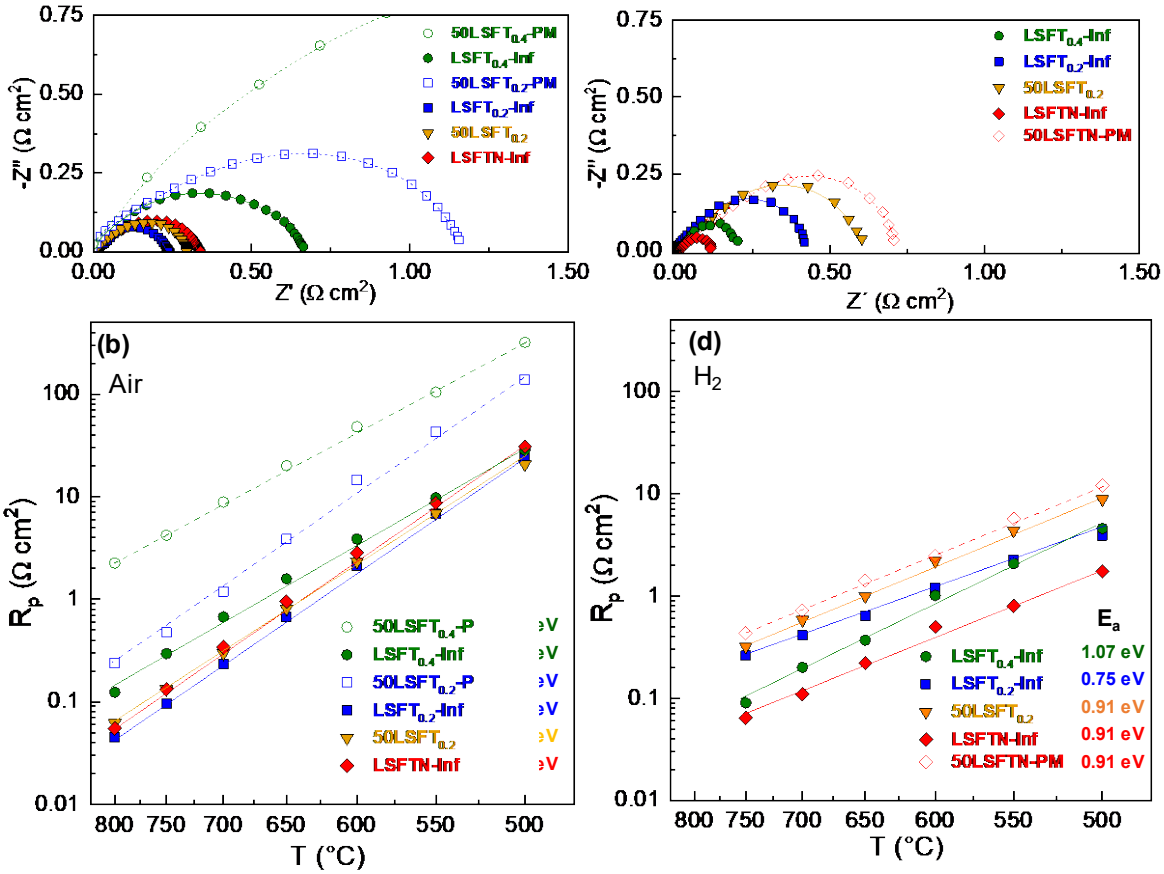

Figure 6. (a) Representative impedance spectra of the different electrode architectures at 700 ºC in air and (b) the corresponding total polarization resistance as a function of the temperature in air. (c) Impedance spectra of the different electrode architectures at 700 ºC in H_2 and (d) the corresponding temperature dependence of the total polarization resistance.

The electrochemical properties of LSFT$_{0.2}$ are significantly improved by microstructural engineering across the entire temperature range studied, resulting in R_p values as low as 0.30 and 0.23 Ω cm^2 for 50LSFT$_{0.2}$ and LSFT$_{0.2}$-Inf at 700 ºC, respectively. Particularly, LSFT$_{0.4}$–Inf exhibits R_p values of 0.67 Ω cm^2 at 700 ºC, clearly outperforming the values obtained for the screen-printed electrodes (8.84 Ω cm^2 at 700 ºC), though they still remain relatively high for considering them as air electrodes (Figure 6a,b). Comparatively, these R_p values are better to those observed in air for other Sr-rich related electrodes, such as

$SrFe_{0.9}Ti_{0.1}O_{3-\delta}$ (2.34 Ω cm^2 at 700 ºC),[60] and $La_{0.3}Sr_{0.7}Fe_{0.7}Ti_{0.3}O_{3-\delta}$ (0.11 Ω cm^2 at 800 ºC), [18] as well as compositions with active exsolved metals, like $Sm_{0.70}Sr_{0.20}Fe_{0.80}Ti_{0.15}Ru_{0.05}O_{3-\delta}$ (0.13 Ω cm^2 at 800 ºC)[61] and $La_{0.7}Sr_{0.3}Ti_{0.1}Fe_{0.6}Ni_{0.3}O_{3-\delta}$ (0.18 Ω cm^2 at 700 ºC) (Table S3).[52]

In wet H_2 atmosphere, $50LSFT_{0.2}$ and $LSFT_{0.2}$-Inf rendered R_p values of 0.58 and 0.41 Ω cm^2, respectively, at 700 ºC, while a lower value of 0.20 Ω cm^2 was obtained for $LSFT_{0.4}$-Inf (Figure 6c,d). The improved electrochemical performance of $LSFT_{0.4}$-Inf can be attributed to its higher electrical conductivity in a reducing atmosphere compared to the electrodes with lower Ti-content. The slight difference in the electrochemical performance between the infiltrated and nanocomposite microstructures, despite the considerably higher extension of the TPB achieved using the latter strategy, may be attributed to the lower porosity in the nanocomposite architecture to the absence of a porous electrolyte backbone. Nevertheless, the fact that similar values were achieved in both atmospheres, compared to the screen-printed sample, supports the implementation of nanocomposite electrodes as the most practical architecture choice. This is primarily because nanocomposite electrodes can be deposited in a single deposition step without the need for a previous backbone deposition, thus simplifying the manufacturing process.

A substantial improvement in the electrochemical performance was achieved with a Ni-doped electrode, $(La_{0.8}Sr_{0.2})_{0.95}(Fe_{0.8}Ti_{0.2})_{0.9}Ni_{0.1}O_{3-\delta}$, deposited by spray-pyrolysis on a CGO backbone (LSFTN-Inf) in H_2 atmosphere, reaching a polarization resistance as low as 0.11 Ω cm^2 at 700 ºC in H_2 (Figure 6c,d). This value represents one of the lowest R_p values for ferrite-based materials to date. Notably, these R_p values are lower than those reported for related materials such as $La_{0.3}Sr_{0.7}Ti_{0.3}Fe_{0.7}O_{3-\delta}$ (0.75 Ω cm^2 at 700 ºC)[62] and $La_{0.3}Sr_{0.7}Fe_{0.9}Ti_{0.1}O_{3-\delta}$ (0.58 Ω cm^2 at 700 ºC),[10] or other compositions with exsolved metals particles, such as $La_{0.7}Sr_{0.3}Ti_{0.1}Fe_{0.6}Ni_{0.3}O_{3-\delta}$ (0.40 Ω cm^2 at 700 ºC) (Table S3).[52] In comparison, the values obtained for LSFTN-Inf clearly outperformed those obtained for the analogous composition prepared by screen-printing (0.70 Ω cm^2 at 700 ºC). The improved R_p for this electrode is clearly attributed to its optimized electrode architecture combined with the exsolution of Ni nanoparticles under reducing conditions. Interestingly, LSFTN-Inf considerably improves the electrochemical activity for fuel oxidation, while a similar performance was observed in air atmosphere. These results demonstrate the crucial role of tailoring the electrode microstructure to enhance the electrochemical performance by increasing the TPB length.

The electrochemical processes involved in the ORR of 50LSFT$_{0.2}$ and LSFT$_{0.2}$-Inf were identified by analyzing the impedance spectra as a function of the pO_2 (Figure 7a and b). The relationship between the resistance of each particular electrode response and pO_2 is expressed as follows: $R_i \sim pO_2^{-m}$, where the value of m provides information about the nature of the species involved in the ORR sub-reactions. The different electrode processes present in the spectra were analysed using the distribution of relaxation times (DRT) technique (Figure 7c,d).[63]

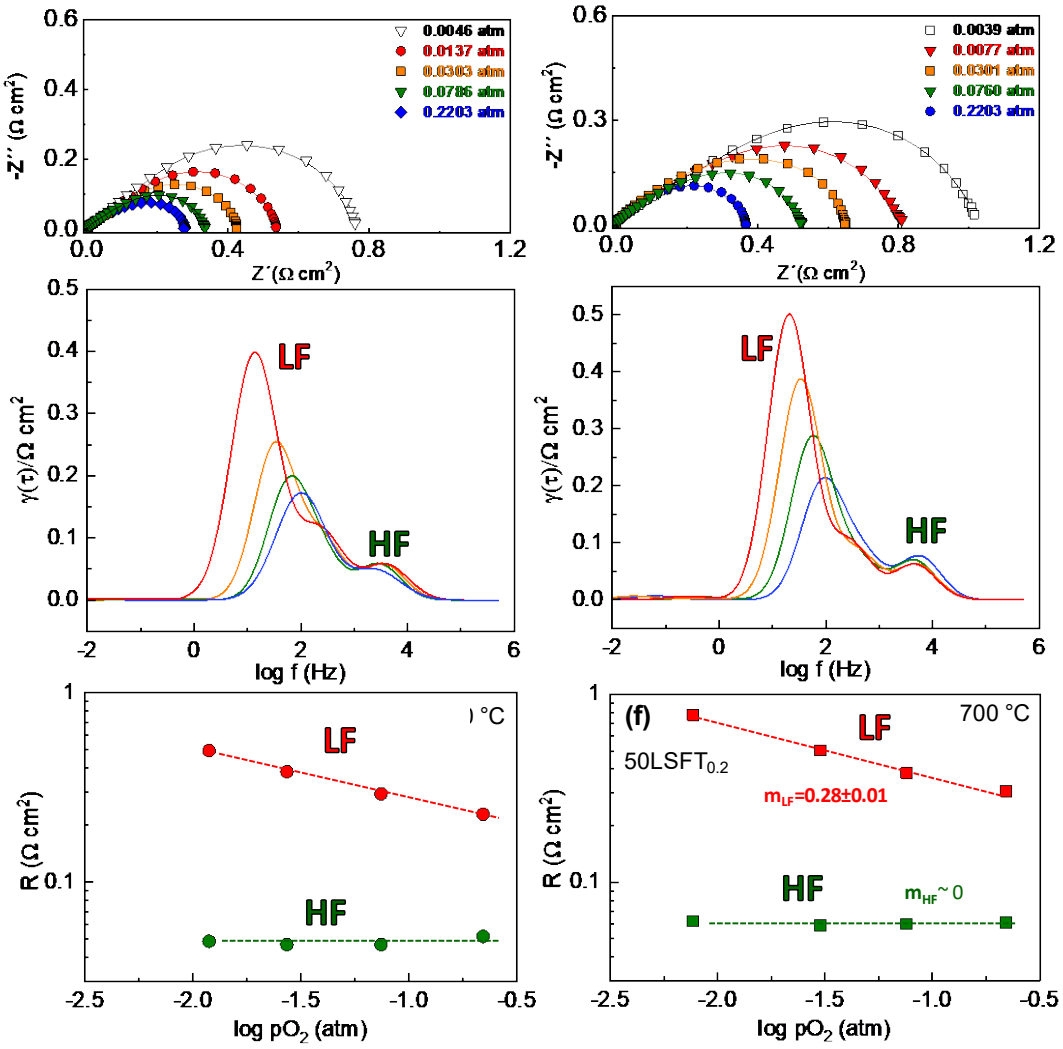

Figure 7. Impedance spectra as a function of the oxygen partial pressure (pO_2) for (a) LSFT$_{0.2}$-Inf, and (b) 50LSFT$_{0.2}$ and (c,d) the corresponding DRT spectra. (e,f) pO_2-dependence of the electrodes resistance contributions.

For both 50LSFT$_{0.2}$ and LSFT$_{0.2}$-Inf electrodes, two distinct electrode processes are discernible. The electrode response at high frequency (HF) remains nearly independent of the pO_2 and can be assigned to the oxygen ion transport at the electrode/electrolyte interface

($O^x_{o,\ electrode} \rightarrow O^x_{o,\ electrolyte}$)[64] (Figure 7c,d). On the other hand, the resistance at low frequency (LF) with a reaction order of m=1/4 can be attributed to charge transfer at the electrode surface ($O_{ad} + 2e^- + V^{\cdot\cdot}_o \rightarrow O^x_o$)[65] (Figure 7e,f). In addition, the LF electrode response shifts to a higher frequency as the pO_2 increases, implying a lower relaxation time and faster electrode kinetics. Within the studied pO_2 range, the LF contribution is the rate-limiting step for ORR. Interestingly, both electrodes exhibit the same contributions, revealing that the different electrode architectures do not significantly alter the limiting steps for ORR.

The electrode polarization was also investigated as a function of the dc-current bias in a three-probe electrode configuration under cathodic and anodic polarization (Figure 8a,b). When a cathodic polarization is applied, the R_p of $LSFT_{0.2}$-Inf significantly decreases from 2.6 Ω cm^2 at open circuit voltage (OCV) to 1.56 Ω cm^2 at −0.4 V at 600 °C (Figure 8a). This improvement is commonly attributed to the formation of additional oxygen vacancies due to a decrease of pO_2 under cathodic current, resulting in enhanced oxide ion conduction.[66] In general, a further reduction in R_p is observed when the dc bias is reversed to anodic mode, reaching 0.42 Ω cm^2 at +0.4 V at 600 °C (Figure 8b).

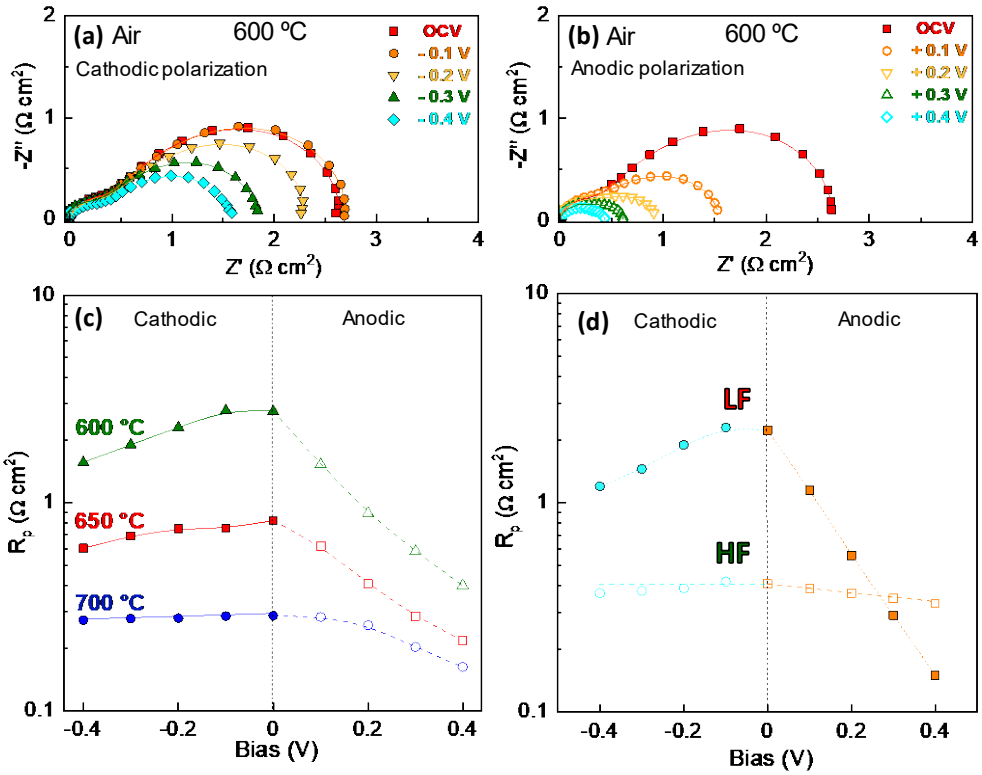

Figure 8. Impedance spectra at 600 °C of $LSFT_{0.2}$-Inf at different dc bias under: (a) cathodic and (b) anodic polarization in a three-probe configuration in air. (c) Overall electrode polarization resistance as a function of the dc bias at different temperatures. (d) Variation of the HF and LF electrode contributions as a function of the dc bias at 600 °C.

This improved performance under anodic polarization has been previously associated with an increase of the pO_2 in the oxygen electrode, which improves the electron-hole conductivity.[67] However, the impact of dc bias on the electrochemical response diminishes at higher temperatures (Figure 8c). At intermediate temperatures, where the oxygen reduction kinetics and oxide-ion transport are slower, the application of a dc bias significantly increases the concentration of oxygen vacancies at the active sites, leading to a considerable improvement in the electrode performance. However, at higher temperatures, the intrinsic ionic conductivity of the electrodes becomes more dominant, reducing the influence of dc polarization on the formation of oxygen vacancies.[66]

To gain further insights into the influence of the dc bias on each electrode response, the impedance spectra were deconvoluted by DRT technique (Figure 8d and Figure S9). The HF contribution, previously attributed to oxide-ion transport at the interface, remains unaffected by the applied dc current due to the excellent mixed ionic-electronic conductivity of the nanoengineered electrode and the rapid charge transfer process at the electrode/electrolyte interface. Interestingly, the LF contribution, associated with electrochemical processes at the electrode surface, suffers a significant decrease at intermediate temperatures under a dc bias, following a similar trend to that observed with changes in pO_2. These findings strongly indicate that the application of a dc bias plays a key role in modulating the concentration of oxygen vacancy, thereby improving the electrochemical properties of the electrodes.

3.4. Fuel cell tests

The efficiency of 50LSF$T_{0.2}$-P, LSF$T_{0.2}$-Inf and LSFTN-Inf electrodes under real operation conditions was tested in symmetrical cells employing a 300 μm thick LSGM electrolyte (Figure 9). In all symmetrical cells, the open circuit voltage (OCV) is close to the theoretical Nernst potential, 1.1 V, confirming a good gas sealing of the cell.

The single cell with the traditional screen-printed 50LSF$T_{0.2}$-PM composite rendered maximum power densities (MPD) of 309 and 141 mW cm^{-2} at 800 and 700 ºC, respectively, in wet H_2 (Figure 9a). These values were considerably improved by the LSF$T_{0.2}$-Inf infiltrated electrode, deposited by spray-pyrolysis, reaching maximum power densities of 496 and 235 mW cm^{-2} at 800, and 700 ºC, respectively (Figure S10).

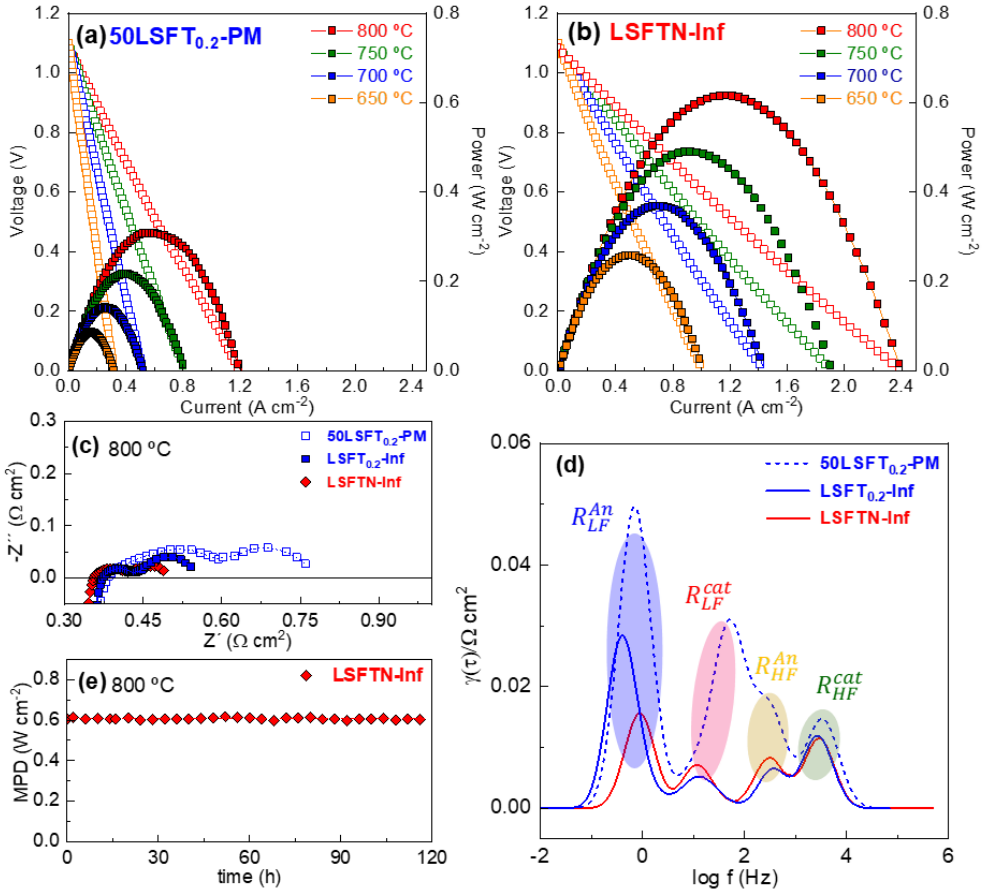

Figure 9. I-V-P curves of different LSGM-supported cell with (a) 50LSFT$_{0.2}$-PM and (b) LSFTN-Inf symmetrical electrodes using wet H_2 as fuel and static air as oxidant. (c) Impedance spectra and (d) the corresponding DRT analysis of the different cell configurations. (e) Stability test of the LSFTN-Inf cell under continuous operation at 800 ºC for 120 h.

Furthermore, the power output was further enhanced for the analogous Ni-containing electrode (LSFTN-Inf), achieving maximum power densities of 617 and 369 mW cm^{-2} at 800 and 700 ºC, respectively (Figure 9b). The incorporation of Ni resulted in superior performance under reducing conditions, due to the formation of highly active exsolved Ni nanoparticles, which provides enhanced HOR kinetics.[24] It is worth highlighting that the power density values of the cell with LSFTN-Inf electrode are higher than those reported in the literature for related compositions, such as 432 mW cm^{-2} at 800 ºC for $La_{0.3}Sr_{0.7}Fe_{0.7}Ti_{0.3}O_{3-\delta}$ onto a 250 µm thick LSGM electrolyte [15] or 471 mW cm^{-2} at 800 ºC for $La_{0.6}Sr_{0.4}Fe_{0.95}Ru_{0.05}O_{3-\delta}$ onto a 300 µm thick LSGM electrolyte [21] (Table S3). Additionally, the cell performance obtained in this work is also comparable or higher than that observed for other nanoengineered symmetrical electrodes, such as $Pr_{0.6}Sr_{0.4}FeO_{3-\delta}$-$PrO_x$ (741 mW cm^{-2} at 800 ºC)[68] or $LaSr_3Fe_2CoO_{10-\delta}$ (351 mW cm^{-2} at 800 ºC)[69] (Table S3).

The similar and close to expected ohmic resistance observed for the different cells, ~0.3 Ω cm^2 at 800 ºC for a 300 µm thick LSGM-supported electrolyte (Figure 9c), clearly highlights that the improved performance can be primarily attributed to two key factors: the higher TPB density of the nanostructured electrodes and the exsolution of Ni nanoparticles. Additionally, it is noteworthy that the ohmic resistance of the cells is higher than the polarization resistance. For instance, in the case of LSFTN-Inf, the ohmic resistance is 0.35 Ω cm^2, while the polarization resistance is 0.14 Ω cm^2 at 800 ºC. These findings suggest that the overall efficiency of the cell is mainly limited by the thickness of the electrolyte. Consequently, higher power output can be achieved by reducing the thickness of the electrolyte.

The DRT spectra reveal that the electrode response comprises four different contributions assigned to the cathode (R^{Cat}) and anode (R^{An}) (Figure 9d). Interestingly, all these processes are reduced for the cell with nanostructured electrodes when compared to the cell with the screen-printed electrode. The low-frequency processes, R^{Cat}_{LF} and R^{An}_{LF}, attributed to electrochemical processes occurring at the cathode and anode surface, respectively, are the main contributions to the overall polarization resistance.[63] These electrode contributions are strongly influenced by the electrode architecture and are significantly decreased through nanoengineering design. These findings are in accordance with the results obtained in the electrode polarization studies in the previous section.

In the case of the $LSFT_{0.2}$-Inf and LSFTN-Inf, very similar electrode contributions were observed for the processes at the electrode/electrolyte interface (R^{Cat}_{HF} and R^{An}_{HF}) and the charge transfer at the cathode surface (R^{Cat}_{LF}). However, the R^{An}_{LF} contribution, attributed to hydrogen oxidation processes at the TPB in the fuel electrode,[70] is considerably decreased for LSFTN-Inf, confirming that the formation of Ni exsolved nanoparticles improves the efficiency for fuel oxidation on the electrode surface.

Additionally, the LSFTN-Inf cell was tested under 5% H_2-Ar to get further information about the fuel electrode contribution (Figure S11). As expected, the R^{An}_{LF} electrode response increased significantly due to the use of diluted hydrogen, confirming the nature of this process. Moreover, LSFTN-Inf displayed excellent stability during continuous operation for over 120 h at 800 ºC (Figure 9e). The analysis of the cross-section of the cell after the electrochemical test further confirmed the stability of the nanostructured electrodes (Figure S12).

Conclusions

Novel electrode compositions, combined with advanced architectural designs, were tested within $(La_{0.8}Sr_{0.2})_{0.95}Fe_{1-x}Ti_xO_{3-\delta}$-$Ce_{0.9}Gd_{0.1}O_{1.95}$ series (x=0.2 and 0.4) to evaluate their potential application in symmetrical solid oxide cells. The nanostructured electrodes, prepared by spray-pyrolysis, exhibited exceptional phase and redox stability. The nanocomposite architecture, featuring nanoscale contact between perovskite and fluorite phases, effectively inhibited the grain growth at high annealing temperatures by suppression cation diffusion at the grain boundary. Moreover, a Ni-doping strategy was found to be highly effective in enhancing the catalytic activity for fuel oxidation, resulting in the formation of highly dispersed exsolved Ni nanoparticles under an H_2 atmosphere. Fuel cell tests conducted on LSGM-supported cells with LSFTN-Inf symmetrical electrodes demonstrated a maximum power density of 611 mW cm^{-2} at 800 ºC in wet H_2, and they also exhibited excellent stability over time. Distribution of relaxation times (DRT) analysis confirmed the significant influence of microstructural tailoring on the superficial electrode processes, mainly due to the extension of the TPB length, thus enhancing electrochemical reactions. These results highlight the critical importance of combining alternative doping strategies and nanostructural optimization to effectively improve the electrode performance in SSOCs.

ASSOCIATED CONTENT

Supporting Information.

XRD patterns of $LSFT_{0.2}$-FD and LSFTN-FD powders; Table with structural parameters for all samples; Rietveld refinements; SEM-EDS analysis of $LSFT_{0.2}$-FD and $LSFT_{0.4}$-FD; XPS analysis of $LSFT_{0.2}$-FD and $LSFT_{0.4}$-FD in oxidizing and reducing conditions; DRT spectra under different dc bias; I-V-P curves of $LSFT_{0.2}$-Inf; Impedance spectra and DRT analysis under 5% and 100% hydrogen; SEM image of the LSGM supported cell after the electrochemical test; Table with R_p and maximum power density values of related compositions.

AUTHOR INFORMATION

Corresponding Author

Javier Zamudio-García - Department of Energy Conversion and Storage, Technical University of Denmark, Fysikvej, Building 310, 2800 Kgs., Lyngby, Denmark. Email: **javzam@dtu.dk**

David Marrero-López - Dpto. de Física Aplicada I, Facultad de Ciencias, Campus de Teatinos, Universidad de Málaga, 29071-Málaga, Spain. Email: **marrero@uma.es**

Author Contributions

The manuscript was written through contributions of all authors. All authors have given approval to the final version of the manuscript.

Notes

The authors declare no competing financial interest.

Acknowledgements

This work was funded by Ministerio de Ciencia, Innovación y Universidades through grants PID2021–126009OB-I00, PID2019-110249RB-I00 and TED2021-129836B-I00. JZG thanks the Ministerio de Ciencia, Innovación y Universidades for his FPU grant (FPU17/02621).

References

(1) Shen, M.; Ai, F.; Ma, H.; Xu, H.; Zhang, Y. Progress and Prospects of Reversible Solid Oxide Fuel Cell Materials. *IScience* **2006**, *24*, 103464. https://doi.org/10.1016/j.isci.2021.103464

(2) Singh, M.; Zappa, D.; Comini, E. Solid Oxide Fuel Cell: Decade of Progress, Future Perspectives and Challenges. *Int. J. Hydrog. Energy*. **2021**, *5*, 27643–27674. https://doi.org/10.1016/j.ijhydene.2021.06.020.

(3) Zakaria, Z.; Awang Mat, Z.; Abu Hassan, S. H.; Boon Kar, Y. A Review of Solid Oxide Fuel Cell Component Fabrication Methods toward Lowering Temperature. *International Journal of Energy Research*. **2020**, *44*, 594–611. https://doi.org/10.1002/er.4907.

(4) Zhang, M.; Du, Z.; Zhang, Y.; Zhao, H. Progress of Perovskites as Electrodes for Symmetrical Solid Oxide Fuel Cells. *ACS Appl. Energy Mater*. **2022**, *28*, 13081–13095. https://doi.org/10.1021/acsaem.2c02149.

(5) Zamudio-García, J.; Caizán-Juanarena, L.; Porras-Vázquez, J. M.; Losilla, E. R.; Marrero-López, D. A Review on Recent Advances and Trends in Symmetrical Electrodes for Solid Oxide Cells. *J. Power Sources*. **2022**, *520*, 230852. https://doi.org/10.1016/j.jpowsour.2021.230852.

(6) Graves, C.; Ebbesen, S. D.; Jensen, S. H.; Simonsen, S. B.; Mogensen, M. B. Eliminating Degradation in Solid Oxide Electrochemical Cells by Reversible Operation. *Nat. Mater.* **2015**, *14*, 239–244. https://doi.org/10.1038/nmat4165.

(7) Bastidas, D. M.; Tao, S.; Irvine, J. T. S. A Symmetrical Solid Oxide Fuel Cell Demonstrating Redox Stable Perovskite Electrodes. *J. Mater. Chem.* **2006**, *16*, 1603–1605. https://doi.org/10.1039/b600532b.

(8) Gu, Y.; Zhang, Y.; Zheng, Y.; Chen, H.; Ge, L.; Guo, L. $PrBaMn_2O_{5+\delta}$ with Praseodymium Oxide Nano-Catalyst as Electrode for Symmetrical Solid Oxide Fuel Cells. *Appl. Catal B.* **2019**, *257*, 117868. https://doi.org/10.1016/j.apcatb.2019.117868.

(9) Qiu, P.; Sun, S.; Li, J.; Jia, L. A Review on the Application of $Sr_2Fe_{1.5}Mo_{0.5}O_6$-Based Oxides in Solid Oxide Electrochemical Cells. *Sep. Purif. Technol.* **2022**, *298*, 121581. https://doi.org/10.1016/j.seppur.2022.121581.

(10) Hou, Y.; Wang, L.; Bian, L.; Wang, Y.; Chou, K. C. Excellent Electrochemical Performance of $La_{0.3}Sr_{0.7}Fe_{0.9}Ti_{0.1}O_{3-\delta}$ as a Symmetric Electrode for Solid Oxide Cells. *ACS Appl. Mater. Interfaces* **2021**, *13*, 22381–22390. https://doi.org/10.1021/acsami.1c02856.

(11) Kaur, P.; Singh, K. Review of Perovskite-Structure Related Cathode Materials for Solid Oxide Fuel Cells. *Ceram. Int.* **2020**, *46*, 5521–5535. https://doi.org/10.1016/j.ceramint.2019.11.066.

(12) Chen, M.; Hu, Y.; Chen, D.; Hu, H.; Xu, Q. A Novel Anode for Solid Oxide Fuel Cells Prepared from Phase Conversion of $La_{0.3}Sr_{0.7}Fe_{0.7}Cr_{0.3}O_{3-\delta}$ Perovskite under Humid Hydrogen. *Electrochim. Acta* **2018**, *284*, 303–313. https://doi.org/10.1016/j.electacta.2018.07.132.

(13) Cai, H.; Zhang, L.; Xu, J.; Huang, J.; Wei, X. L.; Wang, L.; Song, Z.; Long, W. Cobalt–Free $La_{0.5}Sr_{0.5}Fe_{0.9}Mo_{0.1}O_{3-\delta}$ Electrode for Symmetrical SOFC Running on H_2 and CO Fuels. *Electrochim. Acta* **2019**, *320*, 134642. https://doi.org/10.1016/j.electacta.2019.134642.

(14) Li, J.; Wei, B.; Cao, Z.; Yue, X.; Zhang, Y.; Lü, Z. Niobium Doped Lanthanum Strontium Ferrite as A Redox-Stable and Sulfur-Tolerant Anode for Solid Oxide Fuel Cells. *ChemSusChem* **2018**, *11*, 254–263. https://doi.org/10.1002/cssc.201701638.

(15) Liu, L.; Wu, M.; Zhou, X.; Chen, H.; Qian, X.; Wang, Z.; He, F.; Sheng, Y.; Qian, J.; Pan, L. $La_{0.3}Sr_{0.7}Ti_{0.3}Fe_{0.7}O_{3-\delta}$-Based Electrodes for Symmetrical Solid Oxide Fuel Cells by A-Site Deficiency Manipulation. *ACS Appl. Energy Mater.* **2023**, *6*, 841–855. https://doi.org/10.1021/acsaem.2c03142.

(16) Shin, T. H.; Ida, S.; Ishihara, T. Doped CeO_2-$LaFeO_3$ Composite Oxide as an Active Anode for Direct Hydrocarbon-Type Solid Oxide Fuel Cells. *J. Am. Chem. Soc.* **2011**, *133*, 19399–19407. https://doi.org/10.1021/ja206278f.

(17) Zhang, L.; Li, Y.; Zhang, B.; Wan, Y.; Xu, Z.; Zhang, S.; Zhu, T.; Xia, C. $(La,Sr)(Ti,Fe)O_{3-\delta}$ Perovskite with in-Situ Constructed $FeNi_3$ Nanoparticles as Fuel Electrode for Reversible Solid Oxide Cell. *Int. J. Energy. Res.* **2021**, *45* (15), 21264–21273. https://doi.org/10.1002/er.7177.

(18) Cao, Z.; Zhang, Y.; Miao, J.; Wang, Z.; Lü, Z.; Sui, Y.; Huang, X.; Jiang, W. Titanium-Substituted Lanthanum Strontium Ferrite as a Novel Electrode Material for Symmetrical Solid Oxide Fuel Cell. *Int. J. Hydrog. Energy* **2015**, *40*, 16572–16577. https://doi.org/10.1016/j.ijhydene.2015.10.010.

(19) Tang, Y.; Wang, H.; Wang, R.; Liu, Q.; Yan, Z.; Xu, L.; Liu, X. Synergistically Promoting Coking Resistance of a $La_{0.4}Sr_{0.4}Ti_{0.85}Ni_{0.15}O_{3-\delta}$ Anode by Ru-Doping-Induced Active Twin

Defects and Highly Dispersed Ni Nanoparticles. *ACS App.l Mater. Interfaces* **2022**, *14*, 44002–44014. https://doi.org/10.1021/acsami.2c15337.

(20) Marcucci, A.; Zurlo, F.; Sora, I. N.; Placidi, E.; Casciardi, S.; Licoccia, S.; Di Bartolomeo, E. A Redox Stable Pd-Doped Perovskite for SOFC Applications. *J. Mate.r Chem. A* **2019**, *7*, 5344–5352. https://doi.org/10.1039/c8ta10645b.

(21) Marasi, M.; Panunzi, A. P.; Duranti, L.; Lisi, N.; Di Bartolomeo, E. Enhancing Oxygen Reduction Activity and Structural Stability of $La_{0.6}Sr_{0.4}FeO_{3-\delta}$ by 1 Mol % Pt and Ru B-Site Doping for Application in All-Perovskite IT-SOFCs. *ACS Appl. Energy Mater.* **2022**, *5*, 2918–2928. https://doi.org/10.1021/acsaem.1c03613.

(22) Panunzi, A. P.; Duranti, L.; Luisetto, I.; Lisi, N.; Marelli, M.; Di Bartolomeo, E. Triggering Electrode Multi-Catalytic Activity for Reversible Symmetric Solid Oxide Cells by Pt-Doping Lanthanum Strontium Ferrite. *Chemical Engineering Journal* **2023**, *471*, 144448. https://doi.org/10.1016/j.cej.2023.144448.

(23) Tian, Y.; Yang, C.; Wang, Y.; Xu, M.; Ling, Y.; Pu, J.; Ciucci, F.; Irvine, J. T. S.; Chi, B. Phase Transition with in Situ Exsolution Nanoparticles in the Reduced $Pr_{0.5}Ba_{0.5}Fe_{0.8}Ni_{0.2}O_{3-\delta}$ Electrode for Symmetric Solid Oxide Cells. *J. Mater. Chem. A* **2022**, *10*, 16490–16496. https://doi.org/10.1039/d2ta03395j.

(24) Islam, Q. A.; Paydar, S.; Akbar, N.; Zhu, B.; Wu, Y. Nanoparticle Exsolution in Perovskite Oxide and Its Sustainable Electrochemical Energy Systems. *J Power Sources* **2021**, *492*, 229626. https://doi.org/10.1016/j.jpowsour.2021.229626.

(25) Zhang, W.; Hu, Y. H. Recent Progress in Design and Fabrication of SOFC Cathodes for Efficient Catalytic Oxygen Reduction. *Catal. Today* **2023**, *409*, 71–86. https://doi.org/10.1016/j.cattod.2022.05.008.

(26) Connor, P. A.; Yue, X.; Savaniu, C. D.; Price, R.; Triantafyllou, G.; Cassidy, M.; Kerherve, G.; Payne, D. J.; Maher, R. C.; Cohen, L. F.; Tomov, R. I.; Glowacki, B. A.; Kumar, R. V.; Irvine, J. T. S. Tailoring SOFC Electrode Microstructures for Improved Performance. *Adv. Energy Mater.* **2018**, *8*, 1800120. https://doi.org/10.1002/aenm.201800120.

(27) Kim, S.; Kim, G.; Manthiram, A. A Review on Infiltration Techniques for Energy Conversion and Storage Devices: From Fundamentals to Applications. *Sustainable Energy and Fuels*. **2021**, *5*, 5024–5037. https://doi.org/10.1039/d1se00878a.

(28) Fan, L.; Zhu, B.; Su, P. C.; He, C. Nanomaterials and Technologies for Low Temperature Solid Oxide Fuel Cells: Recent Advances, Challenges and Opportunities. *Nano Energy*. **2018**, 45, 148–176. https://doi.org/10.1016/j.nanoen.2017.12.044.

(29) Zhang, J.; Ricote, S.; Hendriksen, P. V.; Chen, Y. Advanced Materials for Thin-Film Solid Oxide Fuel Cells: Recent Progress and Challenges in Boosting the Device Performance at Low Temperatures. *Adv. Funct. Mater*. **2022**, 32, 2111205. https://doi.org/10.1002/adfm.202111205.

(30) dos Santos-Gómez, L.; Zamudio-García, J.; Porras-Vázquez, J. M.; Losilla, E. R.; Marrero-López, D. Recent Progress in Nanostructured Electrodes for Solid Oxide Fuel Cells Deposited by Spray Pyrolysis. *J. Power Sources*. **2021**, *507*, 230277. https://doi.org/10.1016/j.jpowsour.2021.230277.

(31) Hong, G.; Kim, T. W.; Kwak, M. J.; Song, J.; Choi, Y.; Woo, S. K.; Han, M. H.; Cho, C. H.; Kim, S. D. Composite Electrodes of Ti-Doped $SrFeO_{3-\delta}$ and LSGMZ Electrolytes as Both the Anode and Cathode in Symmetric Solid Oxide Fuel Cells. *J. Alloys. Compd.* **2020**, *846*, 156154. https://doi.org/10.1016/j.jallcom.2020.156154.

(32) Dos Santos-Gómez, L.; Porras-Vázquez, J. M.; Losilla, E. R.; Marrero-López, D. Ti-Doped $SrFeO_3$ Nanostructured Electrodes for Symmetric Solid Oxide Fuel Cells. *RSC Adv* .**2015**, *5* 107889–107895. https://doi.org/10.1039/c5ra23771h.

(33) Zamudio-García, J.; Porras-Vázquez, J. M.; Losilla, E. R.; Marrero-López, D. Efficient Symmetrical Electrodes Based on $LaCrO_3$ via Microstructural Engineering. *J. Eur. Ceram. Soc.* **2022**, *42*, 181–192. https://doi.org/10.1016/j.jeurceramsoc.2021.09.059.

(34) General Structure Analysis System (GSAS) Software LosAlamos National Lab (2004).

(35) X'Pert HighScore Plus Software, v3.0e PANalytical B.V., Amelo, The Netherlands (2012).

(36) Wan, T. H.; Saccoccio, M.; Chen, C.; Ciucci, F. Influence of the Discretization Methods on the Distribution of Relaxation Times Deconvolution: Implementing Radial Basis Functions with DRTtools. *Electrochim Acta* **2015**, *184*, 483–499. https://doi.org/10.1016/j.electacta.2015.09.097.

(37) Zamudio-García, J.; dos Santos-Gómez, L.; Porras-Vázquez, J. M.; Losilla, E. R.; Marrero-López, D. Symmetrical Solid Oxide Fuel Cells Based on Titanate Nanocomposite Electrodes. *J. Eur. Ceram. Soc.* **2023**, *43*, 1548–1558. https://doi.org/10.1016/j.jeurceramsoc.2022.11.059.

(38) Marrero-López, D.; Romero, R.; Martín, F.; Ramos-Barrado, J. R. Effect of the Deposition Temperature on the Electrochemical Properties of $La_{0.6}Sr_{0.4}Co_{0.8}Fe_{0.2}O_{3-\delta}$ Cathode Prepared by Conventional Spray-Pyrolysis. *J. Power Sources* **2014**, *255*, 308–317. https://doi.org/10.1016/j.jpowsour.2014.01.021.

(39) Jørgensen, M. J.; Primdahl, S.; Bagger, C.; Mogensen, M. Effect of Sintering Temperature on Microstructure and Performance of LSM-YSZ Composite Cathodes. *Solid State Ion.* **2001**, 139, 1-11. https://doi.org/10.1016/S0167-2738(00)00818-3.

(40) Ruiz-Morales, J. C.; Marrero-López, D.; Gálvez-Sánchez, M.; Canales-Vázquez, J.; Savaniu, C.; Savvin, S. N. Engineering of Materials for Solid Oxide Fuel Cells and Other Energy and Environmental Applications. *Energy Environ Sci* **2010**, *3*, 1670–1681. https://doi.org/10.1039/c0ee00166j.

(41) Leng, J.; Wang, Z.; Wang, J.; Wu, H. H.; Yan, G.; Li, X.; Guo, H.; Liu, Y.; Zhang, Q.; Guo, Z. Advances in Nanostructures Fabricated: Via Spray Pyrolysis and Their Applications in Energy Storage and Conversion. *Chem. Soc. Rev.* **2019**, *48*, 3015–3072. https://doi.org/10.1039/c8cs00904j.

(42) dos Santos-Gómez, L.; Zamudio-García, J.; Porras-Vázquez, J. M.; Losilla, E. R.; Marrero-López, D. Highly Efficient $La_{0.8}Sr_{0.2}MnO_{3-\delta}$ - $Ce_{0.9}Gd_{0.1}O_{1.95}$ Nanocomposite Cathodes for Solid Oxide Fuel Cells. *Ceram. Int.* **2018**, *44*, 4961–4966. https://doi.org/10.1016/j.ceramint.2017.12.089.

(43) Cao, T.; Kwon, O.; Gorte, R. J.; Vohs, J. M. Metal Exsolution to Enhance the Catalytic Activity of Electrodes in Solid Oxide Fuel Cells. *Nanomaterials* **2020**, *10*, 1–23. https://doi.org/10.3390/nano10122445.

(44) Kwon, O.; Joo, S.; Choi, S.; Sengodan, S.; Kim, G. Review on Exsolution and Its Driving Forces in Perovskites. *J. Phys Energy* **2020**, 2, 032001. https://doi.org/10.1088/2515-7655/ab8c1f.

(45) Lu, X.; Yang, Y.; Ding, Y.; Chen, Y.; Gu, Q.; Tian, D.; Yu, W.; Lin, B. Mo-Doped $Pr_{0.6}Sr_{0.4}Fe_{0.8}Ni_{0.2}O_{3-\delta}$ as Potential Electrodes for Intermediate-Temperature Symmetrical Solid Oxide Fuel Cells. *Electrochim. Acta* **2017**, *227*, 33–40. https://doi.org/10.1016/j.electacta.2016.12.170.

(46) Tao, H.; Xie, J.; Wu, Y.; Wang, S. Evaluation of $PrNi_{0.4}Fe_{0.6}O_{3-\delta}$ as a Symmetrical SOFC Electrode Material. *Int. J. Hydrog. Energy* **2018**, *43*, 15423–15432. https://doi.org/10.1016/j.ijhydene.2018.06.047.

(47) Takahashi, Y.; Suzuki, T.; Kawahara, A.; Ando, Y.; Hirano, M.; Shin, W. Dilatometry and High-Temperature X-Ray Diffractometry Study of $La_{0.6}Sr_{0.4}Ti_{0.1}Fe_{0.9}O_{3-\delta}$ and $La_{0.6}Sr_{0.4}Ti_{0.3}Fe_{0.7}O_{3-\delta}$ Oxygen-Permeable Membranes. *Solid State Ion.* **2010**, *181*, 1516–1520. https://doi.org/10.1016/j.ssi.2010.08.024.

(48) Zamudio-García, J.; Porras-Vázquez, J. M.; Canales-Vázquez, J.; Cabeza, A.; Losilla, E. R.; Marrero-López, D. Relationship between the Structure and Transport Properties in the $Ce_{1-x}La_xO_{2-x/2}$ System. *Inorg. Chem.* **2019**, *58*, 9368–9377. https://doi.org/10.1021/acs.inorgchem.9b01104.

(49) Bian, L.; Duan, C.; Wang, L.; O'Hayre, R.; Cheng, J.; Chou, K. C. Ce-Doped $La_{0.7}Sr_{0.3}Fe_{0.9}Ni_{0.1}O_{3-\delta}$ as Symmetrical Electrodes for High Performance Direct Hydrocarbon Solid Oxide Fuel Cells. *J. Mater. Chem A* **2017**, *5*, 15253–15259. https://doi.org/10.1039/c7ta03001k.

(50) Fagg, D. P.; Kharton, V. V.; Frade, J. R.; Ferreira, A. A. L. Stability and Mixed Ionic-Electronic Conductivity of (Sr,La)(Ti,Fe)$O_{3-\delta}$ Perovskites. *Solid State Ion.* **2003**, *156*, 45–57. https://doi.org/10.1016/S0167-2738(02)00257-6.

(51) Zhang, Y.; Shen, L.; Wang, Y.; Du, Z.; Zhang, B.; Ciucci, F.; Zhao, H. Enhanced Oxygen Reduction Kinetics of IT-SOFC Cathode with $PrBaCo_2O_{5+\delta}/Gd_{0.1}Ce_{1.9}O_{2-\delta}$ coherent Interface. *J. Mater Chem A* **2022**, *10*, 3495–3505. https://doi.org/10.1039/d1ta09615j.

(52) Hanif, M. B.; Gao, J. T.; Shaheen, K.; Wang, Y. P.; Yasir, M.; Zhang, S. L.; Li, C. J.; Li, C. X. Performance Evaluation of Highly Active and Novel $La_{0.7}Sr_{0.3}Ti_{0.1}Fe_{0.6}Ni_{0.3}O_{3-\delta}$ Material Both as Cathode and Anode for Intermediate-Temperature Symmetrical Solid Oxide Fuel Cell. *J. Power Sources* **2020**, *472*, 228498. https://doi.org/10.1016/j.jpowsour.2020.228498.

(53) Alvarado Flores, J. J.; Ávalos Rodríguez, M. L.; Andrade Espinosa, G.; Alcaraz Vera, J. V. Advances in the Development of Titanates for Anodes in SOFC. *Int. J. Hydrog. Energy* **2019**, *4*, 12529–12542. https://doi.org/10.1016/j.ijhydene.2018.05.171.

(54) Wærnhus, I.; Grande, T.; Wiik, K. Surface Exchange of Oxygen in $La_{1-x}Sr_xFeO_{3-\delta}$ (x = 0, 0.1). *Topics in Catalysis* **2011**, *54*, 1009–1015. https://doi.org/10.1007/s11244-011-9712-z.

(55) Mizusaki, J.; Sasamoto, T.; Cannon, W. R.; Bowen, H. K. Electronic Conductivity, Seebeck Coefficient, and Defect Structure of $La_{1-x}Sr_xFeO_3$ (X=0.1, 0.25). *J. Am. Ceram. Soc.* **1983**, *66*, 247–252. https://doi.org/10.1111/j.1151-2916.1983.tb15707.x.

(56) Abrantes, J. C. C.; Pérez-Coll, D.; Núñez, P.; Frade, J. R. Electronic Transport in $Ce_{0.8}Sm_{0.2}O_{1.9}$ Ceramics under Reducing Conditions. *Electrochim Acta* **2003**, *48*, 2761–2766. https://doi.org/10.1016/S0013-4686(03)00395-5.

(57) Hou, Y.; Wang, L.; Bian, L.; Zhang, Q.; Chen, L.; Chou, K. chih. Effect of High-Valence Elements Doping at B Site of $La_{0.5}Sr_{0.5}FeO_{3-\delta}$. *Ceram. Int.* **2022**, *48*, 4223–4229. https://doi.org/10.1016/j.ceramint.2021.10.214.

(58) Hu, S.; Zhang, L.; Liu, H.; Cao, Z.; Yu, W.; Zhu, X.; Yang, W. Alkaline-Earth Elements (Ca, Sr and Ba) Doped $LaFeO_{3-\delta}$ Cathodes for CO_2 Electroreduction. *J. Power Sources* **2019**, *443*. https://doi.org/10.1016/j.jpowsour.2019.227268.

(59) Yaremchenko, A. A.; Patrício, S. G.; Frade, J. R. Thermochemical Behavior and Transport Properties of Pr-Substituted $SrTiO_3$ as Potential Solid Oxide Fuel Cell Anode. *J. Power Sources* **2014**, *245*, 557–569. https://doi.org/10.1016/j.jpowsour.2013.07.019.

(60) Baharuddin, N. A.; Mohd Nazrul Aman, N. A.; Muchtar, A.; Somalu, M. R.; Abdul Samat, A.; Aznam, M. I. Structural, Morphological, and Electrochemical Behavior of Titanium-Doped $SrFe_{1-x}Ti_xO_{3-\delta}$ (x = 0.1–0.5) Perovskite as a Cobalt-Free Solid Oxide Fuel Cell Cathode. *Ceram Int* **2019**, *45*, 12903–12909. https://doi.org/10.1016/j.ceramint.2019.03.216.

(61) Fan, W.; Sun, Z.; Bai, Y.; Wu, K.; Zhou, J.; Cheng, Y. In Situ Growth of Nanoparticles in A-Site Deficient Ferrite Perovskite as an Advanced Electrode for Symmetrical Solid Oxide Fuel Cells. *J Power Sources* **2020**, *456*, 228000. https://doi.org/10.1016/j.jpowsour.2020.228000.

(62) Xu, J.; Zhou, X.; Dong, X.; Pan, L.; Sun, K. Catalytic Activity Improvement for Efficient Hydrogen Oxidation of Infiltrated $La_{0.3}Sr_{0.7}Ti_{0.3}Fe_{0.7}O_{3-\delta}$ Anode for Solid Oxide Fuel Cell. *Ceram Int* **2017**, *43* (14), 10750–10756. https://doi.org/10.1016/j.ceramint.2017.05.081.

(63) Osinkin, D. A. An Approach to the Analysis of the Impedance Spectra of Solid Oxide Fuel Cell Using the DRT Technique. *Electrochim Acta* **2021**, *372*, 137858. https://doi.org/10.1016/j.electacta.2021.137858.

(64) Siebert, E.; Hammouche, A.; Kleitz, M. Impedance Spectroscopy Analysis of $La_{1-X}Sr_{itx}MnO_{3-}$ Yttria-Stabilized Zirconia Electrode Kinetics. *Electrochim Acta* **1995**, *40*, 1741–1753. https://doi.org/10.1016/0013-4686(94)00361-4.

(65) Chen, X. J.; Khor, K. A.; Chan, S. H. Identification of O_2 Reduction Processes at Yttria Stabilized Zirconia doped Lanthanum Manganite Interface. *J Power Sources* **2003**, *123*, 17–25. https://doi.org/10.1016/S0378-7753(03)00436-1.

(66) Zapata-Ramírez, V.; Rosendo-Santos, P.; Amador, U.; Ritter, C.; Mather, G. C.; Pérez-Coll, D. Optimisation of High-Performance, Cobalt-Free $SrFe_{1-x}Mo_xO_{3-\delta}$ Cathodes for Solid Oxide Fuel Cells Prepared by Spray Pyrolysis. *Renew Energy* **2022**, *185*, 1167–1176. https://doi.org/10.1016/j.renene.2021.12.121.

(67) Wang, J.; Yang, T.; Lei, L.; Huang, K. Ta-Doped $SrCoO_{3-\delta}$ as a Promising Bifunctional Oxygen Electrode for Reversible Solid Oxide Fuel Cells: A Focused Study on Stability. *J Mater Chem A* **2017**, *5*, 8989–9002. https://doi.org/10.1039/c7ta02003a.

(68) Admasu Beshiwork, B.; Sirak Teketel, B.; Luo, X.; Tian, D.; Yang, Q.; Zhu, S.; Chen, Y.; Timurkutluk, B.; Lin, B. Nanoengineering Electrode for Yttria-Stabilized Zirconia-Based Symmetrical Solid Oxide Fuel Cells to Achieve Superior Output Performance. *Sep. Purif. Technol.* **2022**, *295*, 121174. https://doi.org/10.1016/j.seppur.2022.121174.

(69) Zhou, S.; Yang, Y.; Chen, H.; Ling, Y. In Situ Exsolved Co–Fe Nanoparticles on the Ruddlesden-Popper-Type Symmetric Electrodes for Intermediate Temperature Solid Oxide Fuel Cells. *Ceram. Int* .**2020**, *46*, 18331–18338. https://doi.org/10.1016/j.ceramint.2020.05.057.

(70) Osinkin, D. A. Detailed Analysis of Electrochemical Behavior of High–Performance Solid Oxide Fuel Cell Using DRT Technique. *J. Power Sources* **2022**, *527*, 231120. https://doi.org/10.1016/j.jpowsour.2022.231120.